Nanobody-Driven Stabilization Synergistically Rescues F508del-CFTR and Reveals an Alternative Active State of the Channel

Marie Overtus[1], Tihomir Rubil[2,3,4], James N. Charlick[5], Andrew S. Paige[6], Blaine J. Loughlin[6], Zachary Rich[6], Mayuree Rodrat[5,7], Zhengrong Yang[8], Anita Balázs[2,3,4], John C. Kappes[8], Marcus A. Mall[2,3,4], David N. Sheppard[5], John F. Hunt[6] and Cédric Govaerts[1*]

[1]Biochemistry and Structural Biology, Université Libre de Bruxelles, Campus Plaine, Boulevard du Triomphe, CP206/02, BC building, 1050 Brussels, Belgium.

[2]Department of Pediatric Respiratory Medicine, Immunology and Critical Care Medicine, Charité - Universitätsmedizin Berlin, Berlin, Germany

[3]German Center for Lung Research (DZL), associated partner site Berlin, Berlin, Germany

[4]German Center for Child and Adolescent Health (DZKJ), partner site Berlin, Berlin, Germany

[5]School of Physiology, Pharmacology and Neuroscience, University of Bristol, Bristol, UK.

[6]Fairchild Center, Department of Biological Sciences, Columbia University, New York, NY, USA.

[7]Center for Advanced Therapeutics, Institute of Molecular Biosciences, Mahidol University, Nakhon Pathom, Thailand

[8]Heersink School of Medicine, University of Alabama at Birmingham, Department of Medicine, Birmingham, AL, USA.

* Corresponding author: cedric.govaerts@ulb.be

SUMMARY

Defects in protein trafficking underlie many genetic diseases, including cystic fibrosis (CF), where the common F508del mutation destabilizes the cystic fibrosis transmembrane conductance regulator (CFTR) channel, leading to its degradation. To enhance current CFTR modulator therapies, we used lipid nanoparticles to deliver mRNA encoding T2a, a nanobody that thermally stabilizes CFTR by binding nucleotide-binding domain 1 (NBD1). When combined with clinically-approved correctors, T2a significantly improved F508del-CFTR maturation, plasma membrane expression, and channel activity. Single-channel recording revealed that nanobody binding sustained channel activity by promoting both full and sub-conductance gating states and protecting F508del-CFTR against thermal deactivation. Cryo-EM analysis identified a novel conformation of CFTR where NBD1 adopts an alternative geometry enabling pore formation in the absence of NBD dimerization. Our findings establish a new paradigm to correct protein trafficking by stabilizing misfolded domains with targeted nanobodies and demonstrate a broadly applicable framework to treat CF and related protein misfolding diseases.

INTRODUCTION

Membrane protein trafficking from the endoplasmic reticulum to the plasma membrane involves a series of complex processes to ensure correct protein folding and maturation. Loss-of-function genetic disorders may disrupt protein trafficking, whereby causing insufficient or complete loss of functionality of membrane proteins [1]. The most prevalent protein trafficking disease is cystic fibrosis (CF) where, for most patients, mutations in the CFTR (cystic fibrosis transmembrane conductance regulator) gene severely decrease the plasma membrane expression of this essential epithelial anion channel, perturbing fluid and electrolyte movement, leading to extensive tissue damage in vital organs such as the respiratory airways and digestive system [2, 3].

The CFTR channel has the architecture of ATP-binding cassette (ABC) transporters with two transmembrane domains (TMDs) each composed of six transmembrane (TM) helices connected to two nucleotide-binding domains (NBDs) through structured intracellular loops (ICLs) [4]. Mutations that affect CFTR maturation and trafficking (so-called class II mutations) [5] are found throughout the protein. However, the most prevalent mutation is the deletion of phenylalanine 508 (p.Phe508del; legacy: F508del) [2], located in NBD1, a domain that has been proposed to coordinate CFTR folding [6, 7]. F508del causes thermal instability of NBD1 [8, 9] which, in turn, impairs assembly and stability of the channel [10, 11]. The deleterious impacts of the deletion can be substantially overcome by lowering the temperature during protein biogenesis (i.e. growing F508del-CFTR-expressing cells at 27 °C) [12], an effect that is replicated by introducing compensating mutations into NBD1 [8, 13, 14], which increase its thermal stability. This implies that molecular chaperones which thermally stabilize NBD1 might be important therapeutic assets to treat CF patients bearing class II mutations located in NBD1, particularly F508del [15, 16].

The last decade has seen a revolution in the treatment of CF with the development of CFTR modulators that repair either protein trafficking (correctors) or channel gating (potentiators). The coalescence of two correctors (elexacaftor and tezacaftor) with a potentiator (ivacaftor) in the triple combination therapy elexacaftor-tezacaftor-ivacaftor (ETI) [17] has had transformational benefits for people with CF and F508del [18, 19], leading to the drug's label being extended to 271 other CFTR mutations in the USA (https://www.accessdata.fda.gov/scripts/cder/daf/index.cfm?event=overview.process&ApplNo=212273). While clinical outcomes are overall very positive, some studies have highlighted limitations of the treatment [20-22]. Specifically, in patients bearing at least one F508del mutation, ETI restored CFTR activity to 40-50% of that in non-CF subjects [20]. Such levels of CFTR channel activity parallel those observed in mild forms of CF (showing activities of about 12-54% of controls) [23]. This is supported by the observation that ETI-treated patients do not fully recover lung function and still suffer from chronic lung infection and inflammation [21, 24-26]. In addition, the response to ETI-treatment can vary within a patient cohort, with some patients showing poor improvements, while others do not tolerate the therapy [27]. Thus, further improvement in CFTR function towards full restoration as well as complementary approaches are still needed [28, 29].

Structural studies demonstrate that both of the corrector drugs in the ETI combination therapy bind directly to CFTR at distinct locations within TMD1 [30-32]. Tezacaftor binds in a hydrophobic pocket between TM1, TM2, TM3, TM6, and the C-terminus of the Lasso motif, which plays an important role in CFTR folding [33]. This compound has been hypothesized to stabilize the structural integrity of TMD1 during folding [32]. Elexacaftor binds nearby, making some contacts to TM2 and more extensive contacts to the domain-swapped helices TM10 and TM11 and the N-terminus of the Lasso motif. Of note, these drugs bind at more than 30 Å from F508 indicating that they act allosterically to correct the folding defect caused by that mutation. It was previously proposed based on parallel biophysical [8] and cell biological [14-16] studies that molecules that specifically bind to and thermally

stabilize NBD1 should act as direct CFTR folding correctors, and they could provide a complement or alternative to treat people with CF and the F508del mutation and potentially other class II mutations. We reasoned that such molecular chaperones could be developed from nanobodies that specifically bind and thermally stabilize NBD1. Indeed, we previously isolated a collection of NBD1-specific nanobodies and identified binders with the ability to stabilize both isolated NBD1 and full-length CFTR [34, 35].

Like conventional monoclonal antibodies, nanobodies are being developed as therapeutics for a diverse spectrum of diseases, but always against extracellular targets [36], as exemplified by the first FDA-approved nanobody, caplacimuzab, which binds von Willebrand factor and is used in the treatment of acquired thrombotic thrombocytopenic purpura [37]. For a nanobody to function as a folding chaperone, it must be readily accessible to the newly synthesized polypeptide and bind to the protein during the folding process.

Messenger RNA (mRNA)-based technologies have dramatically reshaped the landscape of protein therapies. The prime example of this transformation is the development of SARS-CoV-2 vaccines where the immunogen (spike protein) was encoded as mRNA encapsulated within lipid nanoparticles (LNPs), enabling efficient delivery of the genetic material to the cell interior. The unprecedented scale and success of SARS-CoV-2 vaccination campaigns have not only showcased the safety and effectiveness of mRNA-based technologies but have also laid the groundwork for their broad application as therapeutics.

Here, we developed an LNP-based strategy to deliver a stabilizing nanobody to cells expressing F508del-CFTR and evaluated its ability to improve protein expression and function. We demonstrated that, by specifically stabilizing NBD1, the nanobody dramatically increases the effects of correctors on F508del-CFTR protein expression and maturation. Using functional studies, we showed that this effect translates into a substantial synergistic improvement in channel activity at the plasma membrane. Cryo-EM studies of CFTR-nanobody complexes demonstrated that the nanobody stabilizes at least two distinct conformations of the protein. In one state, CFTR is locked in an inverted V-shaped inactive state but, remarkably, in the other state the nanobody stabilizes a conformation where detachment of NBD1 enables pore formation in the absence of NBD1-NBD2 dimerization [38], revealing a novel active state of CFTR.

RESULTS

Among our collection of nanobodies, we selected T2a as our chaperone candidate. This nanobody stabilizes both isolated NBD1 and F508del-NBD1 by over 10 °C, as well as purified CFTR by over 8 °C [34]. Crystallography studies have identified that its epitope on NBD1 is relatively large (over 1000 $Å^2$), extending from the core mixed α/β ATP-binding subdomain to the α-helical subdomain of NBD1 [34].

The sequence encoding nanobody T2a was codon-optimized for human expression and mRNA was custom-synthesized by a commercial provider. A C-terminal tag was added to facilitate detection (C-myc or EGFP) (see Methods). To optimize mRNA stability and protein expression, the synthesis included N1-methylpseudouridine (m1ψ) modification, Cap-0 and Cap-1 post-transcriptional modification and a 120a-long polyadenylated tail. For LNP formation, we selected a lipidic composition that included an ionizable lipid (D-Lin-MC3-DMA), a structural phospholipid (DSPC), a sterol (sitosterol) and a pegylated glycerolipid (DMG-PEG 2000) (see Methods), a combination that was described as suitable for lung delivery [39, 40]. Purified mRNA was encapsulated into LNPs using a microfluidic device and physicochemical characteristics of the particles were monitored (see Methods).

mRNA-containing LNPs efficiently deliver the nanobody to the cell interior.

The efficiency of LNP transfection and nanobody expression was tested in cell lines used to evaluate F508del-CFTR trafficking and function, namely HEK293 and the more physiologically relevant CF human bronchial epithelial cells (CFBE41o$^-$) heterologously expressing human F508del-CFTR [41, 42]. We first showed that incubation of HEK293 cells with LNPs led to a dose-dependent expression of the nanobody, with a transfection efficiency of at least 80% (Figure S1).

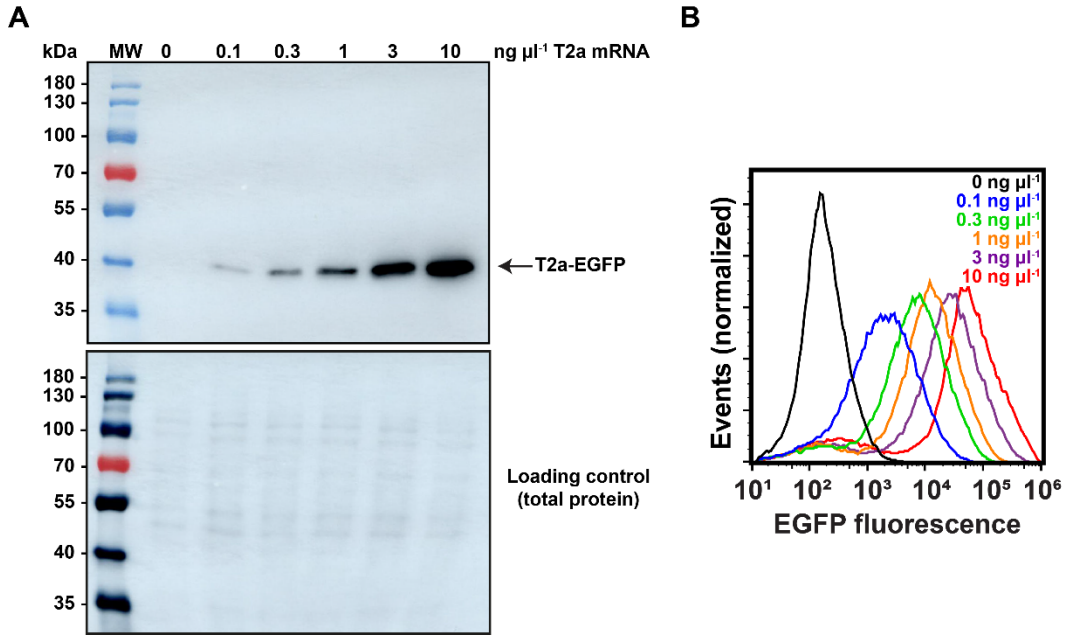

Figure S1. Transfection efficiency of T2a mRNA LNPs
(A) and (B) Dose-response relationship of T2a mRNA LNPs. (A) Top, immunoblot of cell lysates from HEK293; T2a-EGFP was detected with an anti-GFP antibody. Bottom, gel loading control showing total protein amount (Cy5-NHS ester detection). (B) Flow cytometry analysis of T2a nanobody expression using the EGFP tag conjugated to the nanobody. The horizontal axis represents relative total cellular fluorescence, which is proportional to the functional expression level of the T2a-EGFP fusion protein. Data are representative of at least 3 experiments.

Combining approved correctors with nanobody expression substantially increases F508del-CFTR trafficking

To investigate the effect of the T2a nanobody on F508del-CFTR expression and maturation, cells stably expressing F508del-CFTR were incubated with LNPs in the absence or presence of ETI. The efficiency of membrane trafficking was assessed by immunoblotting and densitometric analysis of mature, fully glycosylated CFTR protein (band C). Treatment with nanobody T2a led to little or no visible improvement in band C, while ETI produced a variable but modest increase in band C in HEK293 or CFBE41o$^-$ cells expressing human F508del-CFTR (Figure 1A-D and Figure S2). However, when the two treatments were combined, the increase in mature F508del-CFTR protein was substantially larger in both cell types. For example, even when mature CFTR protein was barely detectable upon overnight treatment of cells with ETI, the combination of ETI and nanobody T2a yielded robust levels of band C (Figure 1A-D and Figure S2). This result indicates that the combination treatment does not lead to a simple

addition of effects but rather a very strong synergy, supporting the molecular modes-of-action of the approved correctors and the stabilizing nanobody being different.

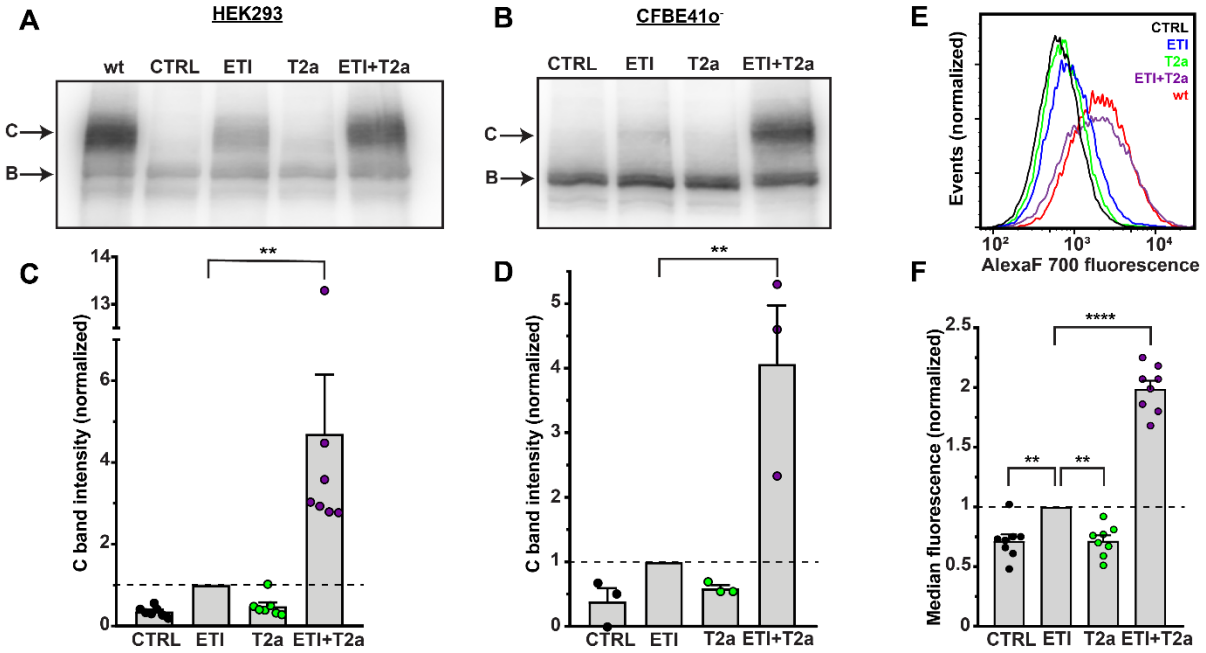

Figure 1. T2a nanobody synergistically improves the efficacy of ETI in correcting the F508del-CFTR maturation defect.

(A) and (B) Maturation of wt and F508del-CFTR. Immunoblots of cell lysates from CFTR-expressing HEK293 (A) and CFBE41o$^-$ (B) cells; both mature (band C) and immature (band B) CFTR forms were visualized with the anti-CFTR monoclonal antibody 596 (recognizing residues 1204-1211 of NBD2 [43]). (C) and (D) Quantification of CFTR maturation. Cells were incubated with 0.3 ng µl^{-1} nanobody T2a mRNA LNPs (T2a) and 3 µM elexacaftor, 18 µM tezacaftor and 3 µM ivacaftor (ETI) either alone or together. Symbols represent individual values and columns means ± SEM (n = 3-7); data were normalized to ETI treatment visually represented by the dashed lines (C band intensity = 1); **, $p < 0.01$; one-way ANOVA. (E) Flow cytometry analyses of the effects of nanobody T2a mRNA LNPs and ETI treatment on F508del-CFTR expression at the plasma membrane of HEK293 cells. An anti-HA antibody and a fluorescently labeled secondary antibody were used to detect the level of plasma membrane expression of CFTR variants harboring a genetically-encoded 3xHA tag in the 4th extracellular loop. For reference, the histogram of the wt-CFTR (red) is also shown. Data were normalized to the number of events acquired in each condition. (F) Quantification of CFTR expression at the plasma membrane. CFTR-expressing HEK293 were treated with 0.3 ng µl^{-1} nanobody T2a mRNA LNP (T2a) and 3 µM elexacaftor, 18 µM tezacaftor and 3 µM ivacaftor (ETI) either alone or together. Symbols represent individual values and columns means ± SEM (n = 8); data were normalized to ETI treatment visually represented by the dashed line (C band intensity = 1); **, $p < 0.01$; ****$p < 0.0001$; one-way ANOVA.

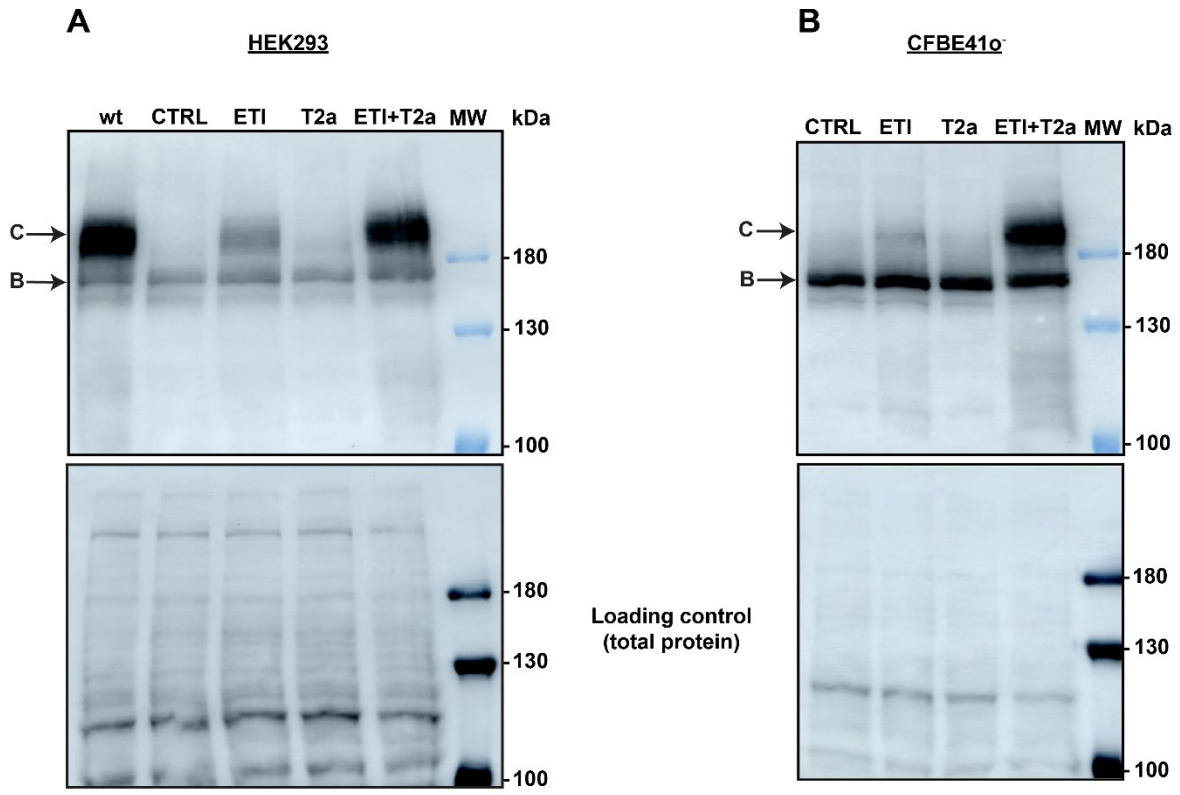

Figure S2. Immunoblots and loading controls for Figure 1 A-B
Top, immunoblots of cell lysates from HEK293 (A) and CFBE41o$^-$ (B) cells; (identical to panels 1 A-B); both mature (band C) and immature (band B) CFTR forms were detected with an anti-CFTR monoclonal antibody 596. Bottom, Cy5-NHS ester detection is used to label the total protein as a loading control of the corresponding immunoblot.

As the HEK293 cells used here express F508del-CFTR with an engineered 3xHA tag in the 4th extracellular loop, we also examined the effect of the treatments on the plasma membrane expression of F508del-CFTR using flow cytometry of cells incubated with an anti-HA antibody and a fluorescent secondary antibody. Gating specifically on non-permeabilized cells, we observed that ETI led to a modest increase in fluorescence, whereas treatment with nanobody T2a mRNA LNPs did not differ from the background fluorescence (Figure 1E and F). However, combining the stabilizing effect of the nanobody with ETI yielded a dramatic increase in plasma membrane expression of F508del-CFTR, reaching a fluorescence signal like that observed in HEK293 cells expressing wild-type CFTR (Figure 1E). Furthermore, the distribution of fluorescence was monomodal, indicating that the combined treatment reached all cells.

Increased maturation of F508del-CFTR translates into enhanced functional rescue.

Next, we tested whether the improvement in F508del-CFTR maturation and expression enhanced the recovery of F508del channel activity. First, we assessed CFTR function with a fluorescence quenching assay using CFBE41o$^-$ cells co-expressing F508del-CFTR and a halide-sensitive yellow fluorescent protein (YFP) [44, 45].

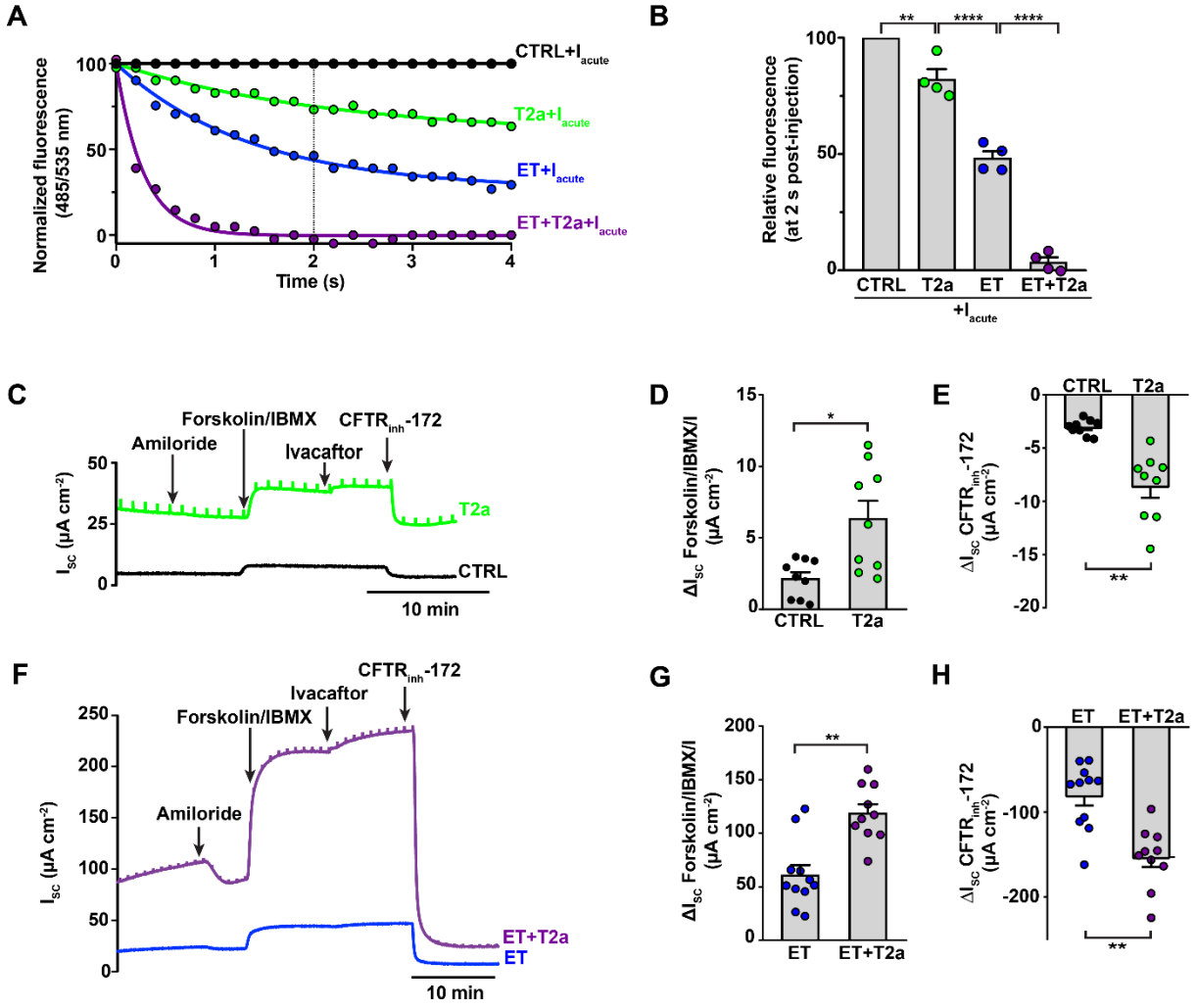

Figure 2. Nanobody T2a mRNA LNPs increase F508del-CFTR activity and synergize with ETI

(A) Halide sensitive-YFP quenching assay to measure F508del-CFTR activity in CFBE41o$^-$ cells co-expressing F508del-CFTR and halide-sensitive YFP. The curves show YFP fluorescence quenching over the first 4 s following iodide injection after treating cells with 10 µM forskolin and 3 µM ivacaftor. Cells were incubated with (i) 2 ng µl^{-1} nanobody T2a mRNA LNPs (T2a), (ii) 3 µM elexacaftor and 18 µM tezacaftor (ET), (iii) T2a and ET (ET+T2a) or untreated (CTRL). (B) Average YFP fluorescence 2 s after iodide injection for the conditions shown in A. Symbols represent individual values and columns are means ± SEM (n = 4); **, $p < 0.01$; ****, $p < 0.0001$; one-way ANOVA. (C) and (F) Representative I_{sc} recordings in CFBE41o$^-$ cells expressing F508del-CFTR. Prior to recordings, CFBE41o$^-$ cells were incubated with either (i) 10 ng µl^{-1} nanobody T2a mRNA LNPs (T2a), (ii) 3 µM elexacaftor and 18 µM tezacaftor (ET), (iii) ET and T2a (ET+T2a) or untreated (CTRL). Arrows indicate the sequential and cumulative addition of amiloride (100 µM), forskolin (10 µM)/IBMX (100 µM), ivacaftor (5 µM) and $CFTR_{inh}$-172 (20 µM) to the apical solution with forskolin/IBMX also added to the basolateral solution. (D), (E), (G) and (H) Quantification of CFTR-mediated forskolin/IBMX/ivacaftor-induced I_{sc} (D and G) and $CFTR_{inh}$-172-sensitive I_{sc} (E and H). Symbols represent individual values and columns are means ± SEM (n = 3-9); *, $p < 0.05$; **, $p < 0.01$; one-way ANOVA.

Figure 2A and B shows that after activating and potentiating F508del-CFTR with forskolin and ivacaftor, addition of iodide to the extracellular medium decreased YFP fluorescence in CFBE41o$^-$ cells treated with nanobody T2a mRNA LNPs compared untreated cells. This effect was stronger when F508del-CFTR was rescued with elexacaftor and tezacaftor (Figure 2A and B). Consistent with our CFTR maturation data (Figure 1), incubating CFBE41o$^-$ with elexacaftor, tezacaftor and nanobody T2a mRNA LNPs led to a much stronger decrease in YFP fluorescence (Figure 2A and B), demonstrating that the synergistic increase of mature F508del-CFTR at the plasma membrane translates into increased channel activity.

To assess F508del-CFTR function with a more physiologically relevant assay, we studied CFTR-mediated Cl^- currents in CFBE41o$^-$ cells with the Ussing chamber technique. CFTR-mediated Cl^- currents were quantified by measuring the change in short-circuit current (I_{sc}) stimulated by cAMP-dependent activation with forskolin/3-isobutyl-1-methylxanthine (IBMX), potentiated by ivacaftor and inhibited with the CFTR inhibitor $CFTR_{inh}$-172. CFTR-mediated Cl^- currents were compared between 4 treatment groups: untreated (CTRL); T2a; ET; and ET+T2a. Paralleling the results observed in the YFP fluorescence assay (Figure 2A and B), treatment of F508del-CFTR-expressing CFBE41o$^-$ cells with nanobody T2a mRNA LNPs modestly, but significantly enhanced CFTR-mediated I_{sc} compared with untreated controls (Figure 2C and D). The correctors elexacaftor and tezacaftor again elicited greater CFTR-mediated I_{sc} than T2a-LNPs alone (Figure 2F and G). Of note, treating F508del-CFTR-expressing CFBE41o$^-$ cells with T2a-LNPs and elexacaftor and tezacaftor led to substantial constitutive CFTR-mediated I_{sc} and doubled the magnitude of forskolin/IBMX/ivacaftor-induced, $CFTR_{inh}$-172-inhibited CFTR-mediated I_{sc} compared with cells treated with correctors alone (Figure 2F-H). Thus, the nanobody T2a rescues F508del-CFTR expression and function in synergy with approved correctors.

T2a modulates channel activity at the single molecule level.

The binding epitope of the T2a nanobody on NBD1 is located within the core ATP-binding α/β subdomain and includes both the Walker A motifs and Walker B loop [34]. This implies that, in the context of full-length CFTR, binding of T2a to the channel would position the nanobody between NBD1 and NBD2, thus sterically preventing their dimerization. However, the ATP-driven NBD dimerization model of CFTR channel gating [38] requires that NBD1-NBD2 dimerization is crucial for gate opening within the TMDs and hence, anion flow. This predicts that T2a binding to CFTR should prevent channel opening in marked contrast to the augmented F508del-CFTR function that we observed when F508del-CFTR-expressing CFBE41o$^-$ cells were treated with CFTR correctors and the nanobody T2a (Figure 2). To investigate this apparent contradiction, we analyzed the modulation of channel activity by T2a at the single molecule level with the patch-clamp technique using excised inside-out membrane patches from BHK cells expressing wild-type or F508del-CFTR. Addition of 1 μM of purified T2a nanobody to the intracellular solution was without effect on current flow through open channels but markedly altered the gating behavior of wt-CFTR (Figures 3A and B, S3A-C). In the absence of nanobody, the channel displayed a bursting pattern of channel gating distinguished by openings interrupted by brief closures, separated by longer closures between bursts (Figures 3A, S3A and S3B), with a stable open probability (P_o) of 0.3 ± 0.02 (n = 4) (Figure S3C). By contrast, the addition of T2a imposed a clear modal gating pattern on wt-CFTR, which alternated between inactive periods (P_o = 0 ± 0; n = 4) and active periods (P_o = 0.4 ± 0.03; n = 4) with little change in overall P_o (Figures 3B, S3A-C). We hypothesize that the inactive periods could represent the conformation where nanobody binding prevents NBD1-NBD2 dimerization and thus channel opening, while the active periods could correspond to either nanobody unbinding or an active conformation that is compatible with both T2a binding and channel opening (see below, single-channel studies of F508del-CFTR). Importantly, the concentration of T2a used in these experiment (1 μM) is more than 2 orders of magnitude greater than the apparent affinity of this nanobody for either isolated NBD1 or full-length CFTR [34], suggesting that the nanobody could be bound to CFTR most of the time.

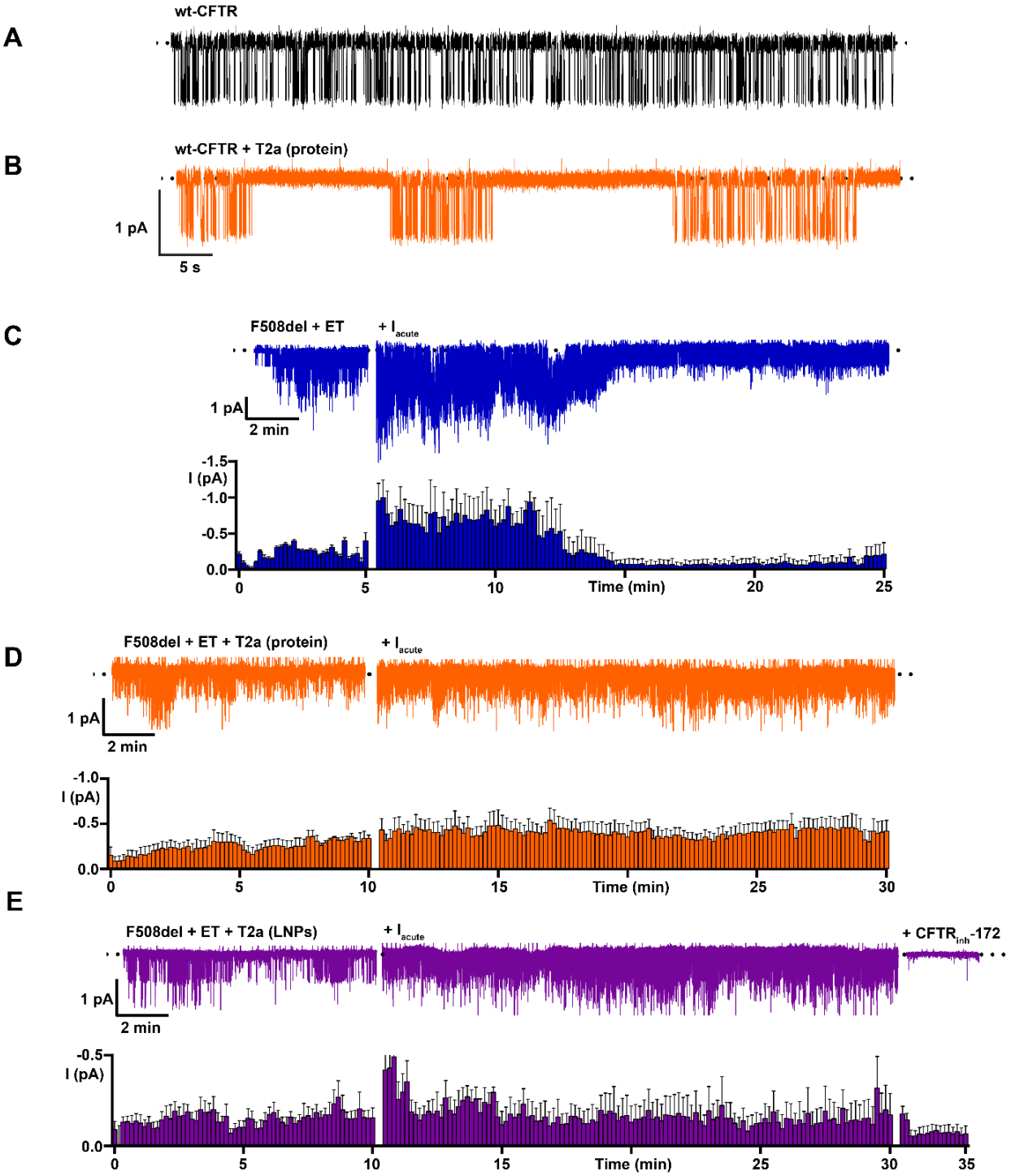

Figure 3. Nanobody T2a modifies the gating behavior of CFTR

(A) and (B) Representative 60 s recordings of a single wt-CFTR Cl^- channel in an excised inside-out membrane patch from a BHK cell stably expressing wt-CFTR acquired in the absence (A) and presence (B) of nanobody T2a (1 μM) in

the intracellular solution. ATP (0.3 mM) and PKA (75 nM) were continuously present in the intracellular solution; temperature was at 37 °C. (C–E) Representative prolonged recordings of F508del-CFTR Cl^- channels in excised inside-out membrane patches from BHK cells stably expressing F508del-CFTR. To increase the plasma membrane expression of F508del-CFTR, BHK cells were treated with elexacaftor (2 µM) and tezacaftor (3 µM) for 24 h at 37 °C prior to study. The recordings were made at 37 °C before and after ivacaftor (1 µM) addition to the intracellular solution, which continuously contained ATP (1 mM) and PKA (75 nM). (C) control recording. (D) Nanobody T2a protein (1 µM) was acutely added to the intracellular solution following channel activation at 25 °C prior to raising the temperature to 37 °C and commencing the recording. (E) The F508del-CFTR-expressing cells were treated with T2a nanobody mRNA LNPs (2 ng μl^{-1}) for 24 h at 37 °C concurrently with elexacaftor and tezacaftor treatment. The recordings were made before and after $CFTR_{inh}$-172 (10 µM) addition to the intracellular solution. Dotted lines indicate the closed channel state and downward deflections correspond to channel openings. Beneath the representative prolonged recordings, the corresponding total current (I) time courses are shown. Data are means ± SEM (n = 4–5) with I values calculated for consecutive 10 s intervals; individual data points are omitted for illustration purposes.

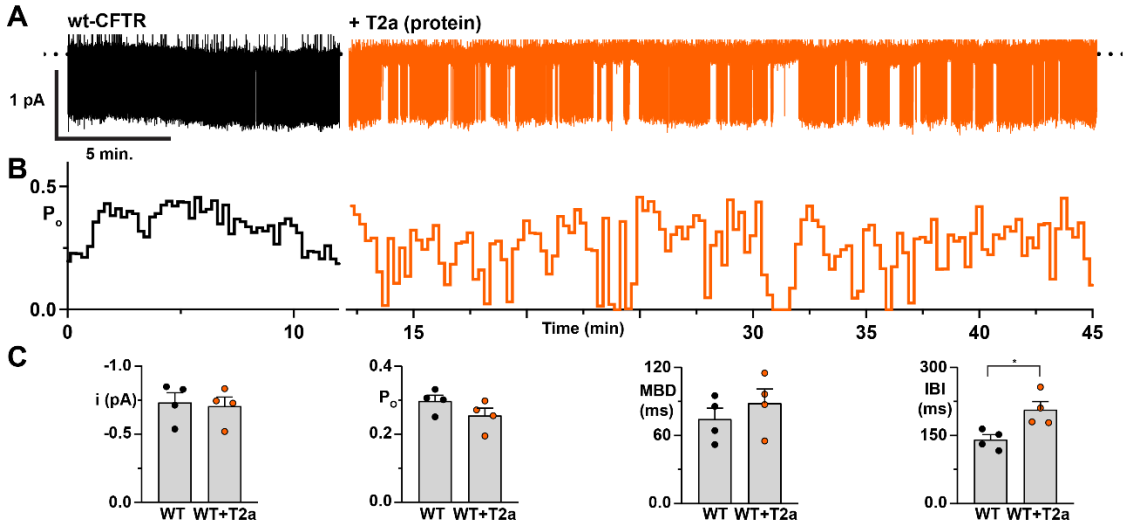

Figure S3. Nanobody T2a modifies the gating behaviour of wt-CFTR
(A) Representative prolonged recordings of a single wt-CFTR Cl^- channel in an excised inside-out membrane patch from a BHK cell stably expressing wild-type CFTR acquired in the absence (black-12 min) and presence (orange-45 min) of nanobody T2a (1 µM) in the intracellular solution. ATP (0.3 mM) and PKA (75 nM) were continuously present in the intracellular solution; temperature was 37 °C. Dotted lines indicate the closed channel state and downward deflections correspond to channel openings. (B) Time courses of open probability (P_o) for the prolonged recordings in A. P_o was calculated for consecutive 15 s periods. (C) Summary single-channel current amplitude (i), open probability (P_o), mean burst duration (MBD) and interburst interval (IBI) of wild-type CFTR determined from prolonged recordings (≥ 10 min) for the experimental conditions described in A and B. Symbols represent individual values and columns are means ± SEM (n = 4); *, P < 0.05 vs. control; two-tailed paired t-test.

We then investigated the single-channel behavior of F508del-CFTR rescued with the correctors elexacaftor and tezacaftor and the nanobody T2a. Membrane patches were excised from cells expressing F508del-CFTR, voltage-clamped at –50 mV in the presence of a Cl^- concentration gradient and channel activity recorded continuously in

the presence of ATP and PKA at 37 °C. When cells were treated with elexacaftor and tezacaftor only, F508del-CFTR showed moderate channel activity that was increased about two-fold by ivacaftor (Figure 3C). However, potentiation of F508del-CFTR by ivacaftor was short-lived with current decreasing to background levels after 10-15 min (Figure 3C). By contrast, when similar measurements were performed in the presence of purified T2a nanobody (1 μM), the activity of F508del-CFTR rescued by elexacaftor and tezacaftor was sustained for the entire duration of prolonged recordings (≥ 30 min) at 37 °C even when channels were potentiated by ivacaftor (Figure 3D). Of note, similar stability of F508del-CFTR at 37 °C was observed when BHK cells were treated with T2a nanobody mRNA LNPs for 24 h at 37 °C concurrently with elexacaftor and tezacaftor (Figure 3E). As observed with our Ussing-chamber experiments (Figure 2), the sustained activity of F508del-CFTR from cells treated with correctors and T2a nanobody mRNA LNPs was inhibited by the CFTR inhibitor $CFTR_{inh}$-172 (Figure 3E). These results demonstrate robust thermodynamic stabilization of F508del-NBD1 at 37 ˚C, a temperature at which it is unstable in the presence of the ATP concentration used in these experiments [8].

When we examined the gating pattern of F508del-CFTR treated with T2a nanobody, we observed openings to sub-conductance states (S-CSs) in addition to those to the full open-state (Figures 4B and C, S4B and C, S6A and B). Indeed, the frequency of S-CS openings was so great in membrane patches treated either acutely with purified T2a nanobody or chronically with T2a nanobody mRNA LNPs that they prevented calculation of P_o to quantify channel gating. To resolve openings of F508del-CFTR to small amplitude S-CSs, we digitally filtered single-channel recordings at 50 Hz, an approach which we have previously used to resolve openings of mouse CFTR to a tiny S-CS [46]. Figure 4A reveals that prior to potentiation with ivacaftor, F508del-CFTR rescued with elexacaftor and tezacaftor predominantly opened to the full open state [single-channel current amplitude (i), –0.68 ± 0.03 pA; n = 4] and rarely to S-CSs (i, –0.21 ± 0.02 pA; n = 4; Figure S6A). By contrast, when F508del-CFTR was treated with T2a nanobody under similar conditions, openings to S-CSs were strongly increased (Figure 4B and C, S6A). Although we observed openings to S-CSs of different amplitudes, we could not distinguish whether these represent openings of a single channel to different S-CSs [47] or S-CS openings of distinct channels because all membrane patches contained several active F508del-CFTR Cl^- channels. Nevertheless, the amplitude of S-CS openings was comparable between F508del-CFTR treated with T2a nanobody either as purified protein or mRNA LNPs and untreated F508del-CFTR controls (Figures 4 and S6A). Moreover, T2a nanobody-treated F508del-CFTR still opened to the full open state and its amplitude was comparable to that observed in the absence of the nanobody (Figures 4B and C, S6). Of note, following potentiation by ivacaftor, openings to S-CSs were even more pronounced for F508del-CFTR treated with T2a nanobody. Figure S4 demonstrates that ivacaftor markedly increased openings of F508del-CFTR Cl^- channels to S-CSs either when channels were acutely treated with purified T2a nanobody or cells chronically incubated with T2a nanobody mRNA LNPs with the result that discrete openings to S-CSs were no longer apparent in single-channel current amplitude histograms. Figures 3 and S4 also show that the T2a nanobody protected F508del-CFTR from thermal deactivation [48]. At 25 min after ivacaftor addition to the intracellular solution, openings to both the full open state and S-CSs were readily apparent in the presence of T2a nanobody, whereas channel activity had deactivated completely in the absence of T2a (Figures 3C-E and S4).

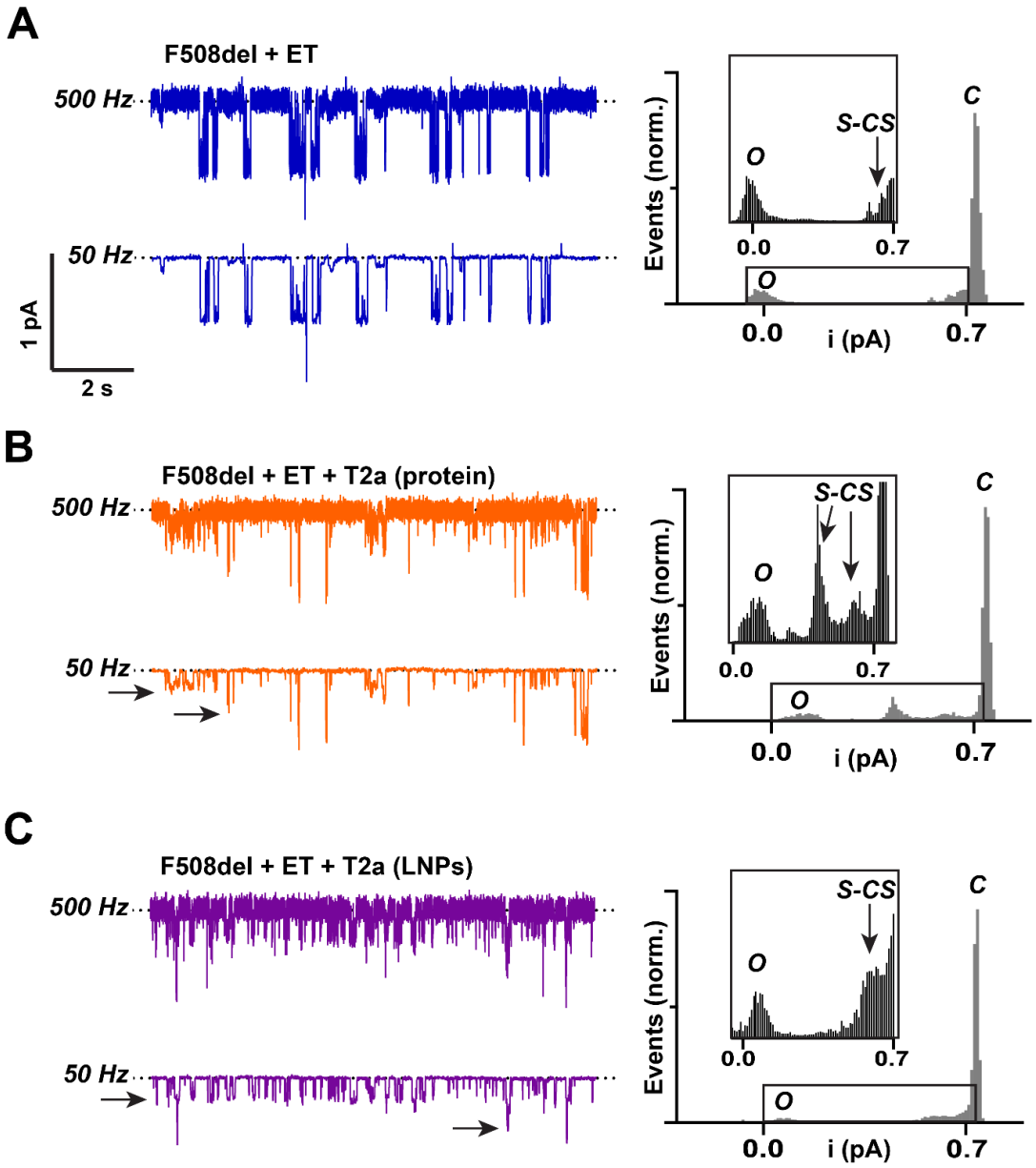

Figure 4. Nanobody T2a promotes opening of F508del-CFTR Cl^- channels to sub-conductance states
(A-C) Left, representative 12 s single-channel recordings of F508del-CFTR before ivacaftor addition for the time course data shown in Figure 3 that were either filtered at 500 Hz or additionally filtered at 50 Hz. Right, 60-s single-channel current amplitude histograms of F508del-CFTR, which include the recordings shown on the left after additional filtering at 50 Hz. Dotted lines indicate the closed channel state and downward deflections correspond to channel openings. The labels C and O denote the closed and full open states of the channel. Regions of current amplitude histograms enclosed by rectangles are enlarged in the insets to highlight openings to sub-conductance states (S-CSs), identified with arrows. (A) Control recording using a membrane patch excised from a BHK cell treated with elexacaftor (2 µM) and tezacaftor (3 µM). (B) Recording in the continuous presence of nanobody T2a (1 µM) in the intracellular solution using a membrane patch excised from a BHK cell treated with elexacaftor and tezacaftor. (C) Recording from a membrane patch excised from a BHK cell treated with T2a nanobody mRNA LNPs (2 ng μl^{-1}) for 24 h at 37 °C concurrently with elexacaftor and tezacaftor treatment.

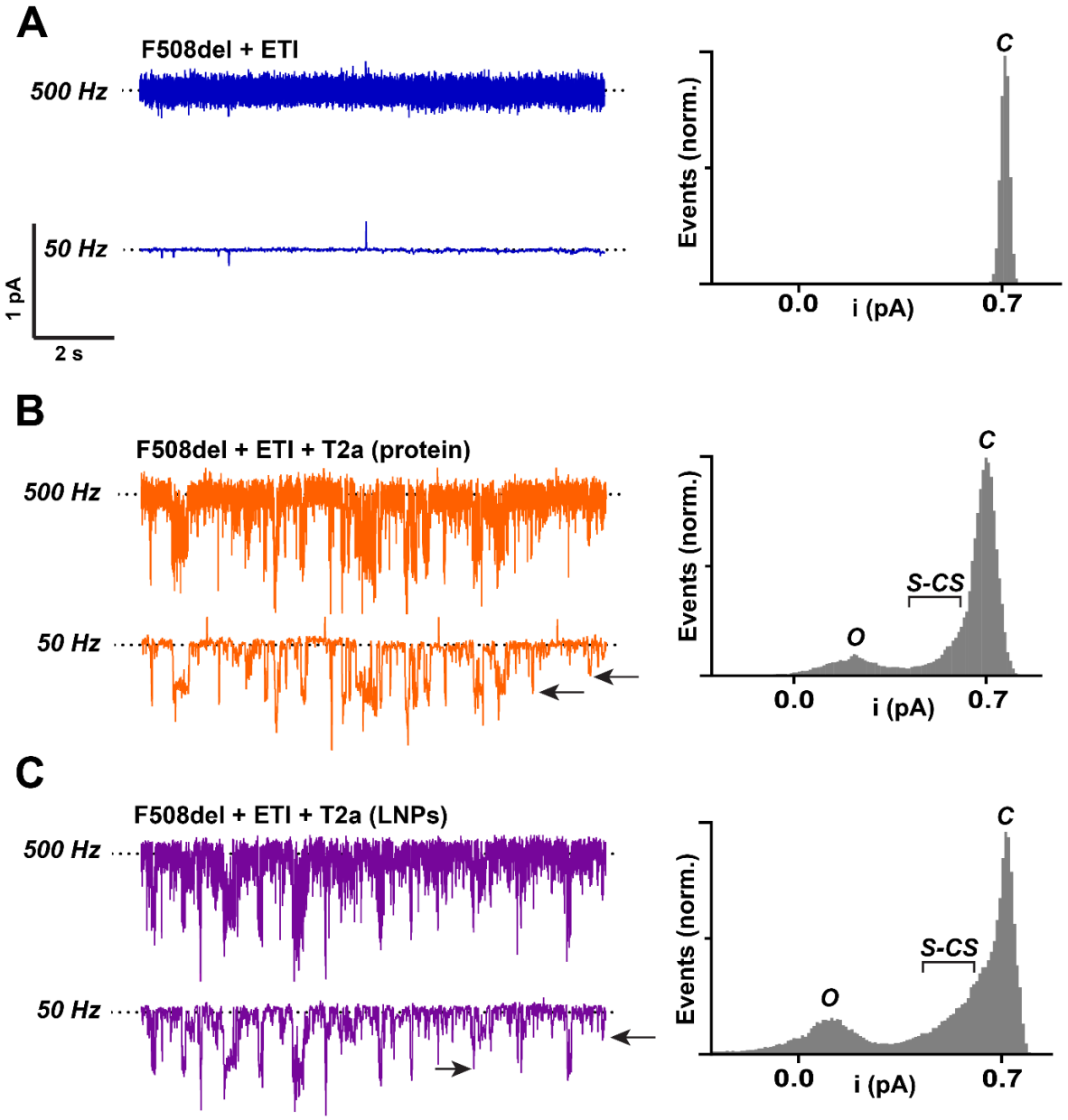

Figure S4. Nanobody T2a-treated F508del-CFTR opens to both the full open and sub-conductance states after prolonged exposure to ivacaftor

(A-C) Left, representative 12 s single-channel recordings of F508del-CFTR 25 min after ivacaftor (1 µM) addition for the time course data shown in Figure 3 that were either filtered at 500 Hz or additionally filtered at 50 Hz. Right, 60-s single-channel current amplitude histograms of F508del-CFTR, which include the recordings shown on the left after additional filtering at 50 Hz. Dotted lines indicate the closed channel state and downward deflections correspond to channel openings. The labels C and O denote the closed and full open states of the channel, while brackets illustrate openings to sub-conductance states (S-CSs). (A) Control recording using a membrane patch excised from a BHK cell treated with elexacaftor (2 µM) and tezacaftor (3 µM). (B) Recording in the continuous presence of nanobody T2a (1 µM) in the intracellular solution using a membrane patch excised from a BHK cell treated with elexacaftor and tezacaftor. (C) Recording from a membrane patch excised from a BHK cell treated with T2a nanobody mRNA LNPs (2 ng μl^{-1}) for 24 h at 37 °C concurrently with elexacaftor and tezacaftor treatment.

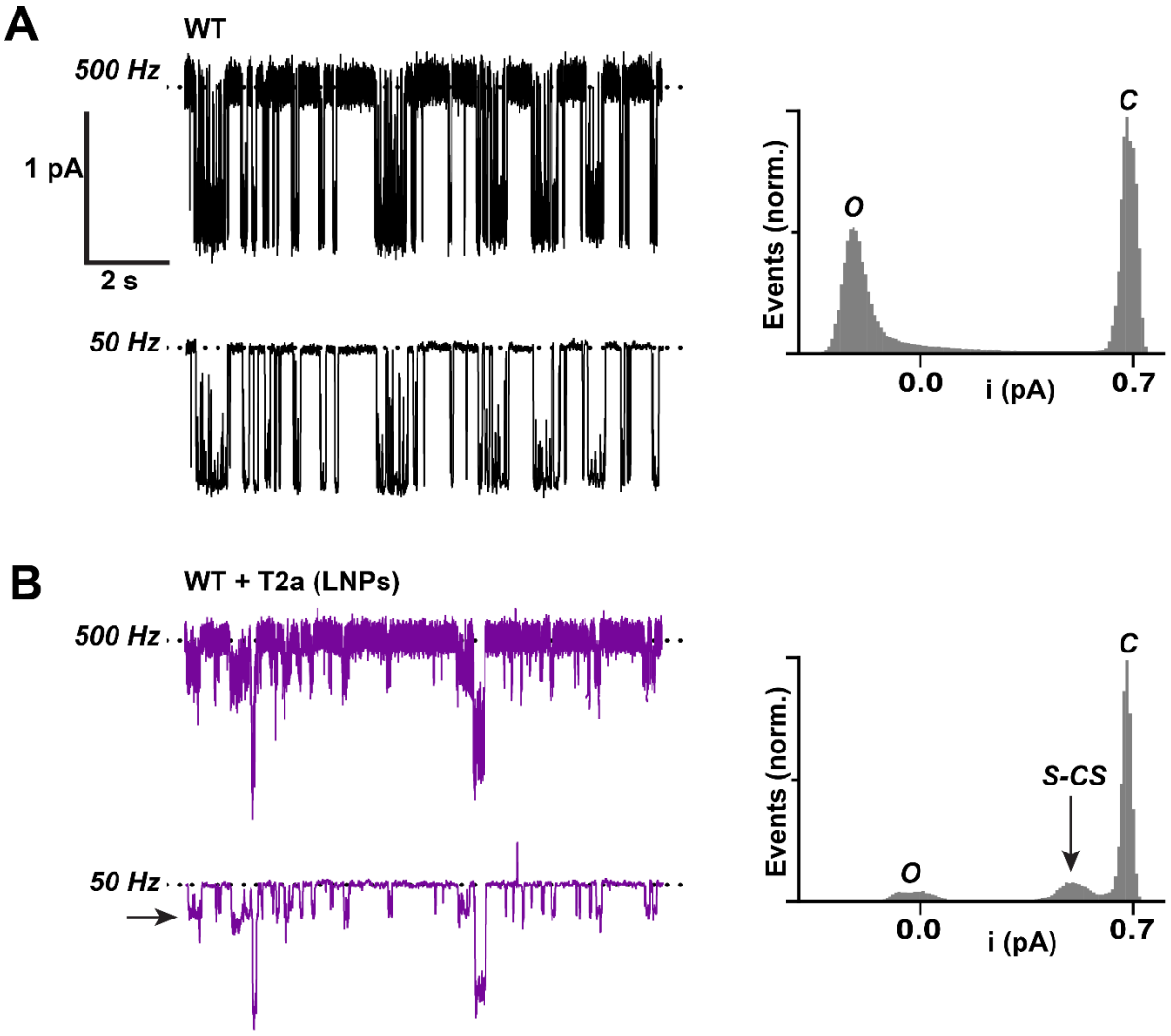

Figure S5. Nanobody T2a-treated wt-CFTR opens to both the full open and sub-conductance states
(A) and (B) Left, representative recordings of wt-CFTR Cl^- channels in excised inside-out membrane patches from BHK cells stably expressing wt-CFTR filtered at 500 Hz or additionally filtered at 50 Hz. (A) Control recording. (B) Recording from a membrane patch excised from a BHK cell treated with T2a nanobody mRNA LNPs (2 ng μl^{-1}) for 24 h at 37 °C. Dotted lines indicate the closed channel state and downward deflections correspond to channel openings. Right, 110-s single-channel current amplitude histograms of the wt-CFTR, which include the recordings shown on the left after additional filtering at 50 Hz. The labels C and O denote the closed and full open states of the channel, while arrows illustrate openings to sub-conductance states (S-CSs).

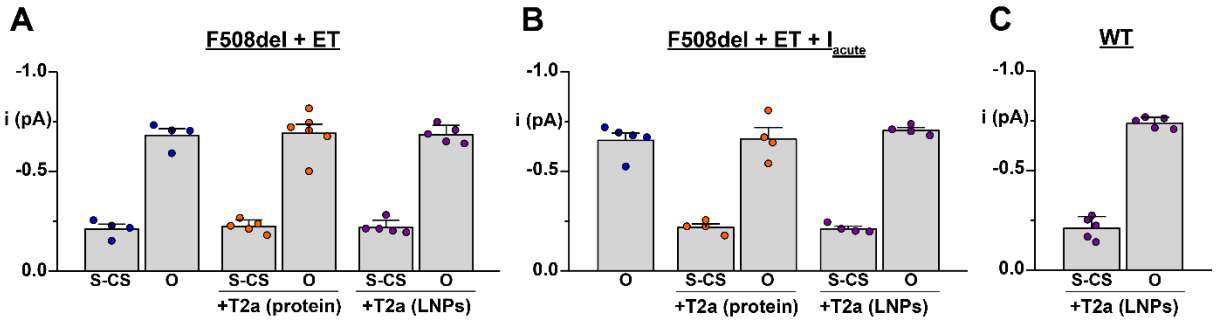

Figure S6. The single-channel current amplitudes of wild-type and F508del-CFTR treated with nanobody T2a
Summary single-channel current amplitude data for the sub-conductance state (S-CS) and full open state (O) of wild-type and F508del-CFTR recorded in excised inside-out membrane patches from BHK cells. Cells expressing F508del-CFTR were chronically treated with elexacaftor (E; 2 µM) and tezacaftor (T; 3 µM) for 24 h at 37 °C while cells expressing wt-CFTR were untreated. Membrane patches were either untreated or treated with nanobody T2a (1 µM) by addition to the intracellular solution during recordings (+T2a protein). Alternatively, membrane patches were excised from cells treated with T2a nanobody mRNA LNPs (2 ng μl^{-1}) for 24 h at 37 °C concurrently with elexacaftor and tezacaftor treatment (+T2a LNPs). (A) Current amplitude data from F508del-CFTR Cl^- channels prior ivacaftor addition. (B) Current amplitude data from F508del-CFTR Cl^- channels acutely treated with ivacaftor (I) following their activation. (C) Current amplitude data from wt-CFTR-expressing cells treated with T2a nanobody mRNA LNPs (2 ng μl^{-1}) for 24 h at 37 °C. Symbols represent individual values and columns means ± SEM (wt-CFTR, n = 4–5; F508del-CFTR control, n = 4–5; F508del-CFTR T2a protein, n = 4–6; F508del-CFTR T2a LNPs, n = 4–5).

The action of the T2a nanobody on F508del-CFTR differs markedly to its action on wt-CFTR, where purified T2a nanobody imposed a modal gating pattern on the channel without inducing openings to S-CSs (Figures 3, 4, S3 and S4). To learn whether nanobody T2a-dependent openings to S-CSs are limited to F508del-CFTR, we treated BHK cells expressing wt-CFTR with T2a nanobody mRNA LNPs. Under these conditions, wt-CFTR opened to both the full open state and S-CSs with the amplitude of S-CSs similar to those observed with F508del-CFTR and that of the full open state comparable to the absence of nanobody T2a (Figures S3, S5 and S6). Thus, our data suggest that both wt- and elexacaftor and tezacaftor-rescued F508del-CFTR chronically treated with T2a nanobody adopt open-pore conformations that mediate either partial or full anion flow through the channel.

Binding of T2a reveals a novel conformation of CFTR

To understand how T2a binding affects the conformation of CFTR to enable channel opening, we used cryo-EM to solve the structure of the complex (Table S1). Human wild-type CFTR (hCFTR) was overexpressed in mammalian cells and purified to homogeneity in digitonin and cholesterol-hemisuccinate (see Methods). Phosphorylated and concentrated CFTR was incubated at 4˚C for 2 h with ATP in the absence or presence of purified T2a nanobody prior to flash-freezing and deposition on cryo-EM grids. After data collection, micrographs were processed and 3-dimensional reconstruction were performed as previously described using cryoSPARC [49, 50] (Figure S7 and Table S1). In the absence of T2a, single-particle analysis produced 3D reconstruction of a cryo-EM map at 3.1 Å resolution enabling reliable model building. This structure of CFTR adopted the “inverted V-shaped” topology where the NBDs are separated by about 20 Å (Figure 5A). Although we did not observe density for the R domain, this conformation is highly similar to the cryo-EM structure previously reported for dephosphorylated ATP-free hCFTR [51] with the two models showing less than 1.8 Å RMSD with most of the differences observed at the level of NBD2 which is slightly rotated (Figure S8A) whereas the TM helices align well.

Table S1. Cryo-EM data collection and refinement statistics for human wt-CFTR structures.

Structure PDB deposition ID EMDB accession code	**V-Shaped+T2a** 9Q1W EMD-72143 [1]	**Alternative NBD1+T2a** 9Y1Q EMD-72403 [2]	**V-Shaped** 9Y4T EMD-72497 [3]
EMPIAR accession code	EMPIAR-12127		EMPIAR-12947
Data collection			
Microscope	KRIOS		KRIOS
Camera	K3		K3
Magnification	105,000		105,000
Voltage (kV)	300		300
Electron exposure (e–/Å^2)	58		58
Defocus range (μm)	0/-2.0		0/-2.0
Pixel size (Å)	0.83		0.83
Symmetry imposed	C1		C1
Micrographs (no.)	11,110		12,863
Initial particles (no.)	886,769 [4]		702,919 [5]
Data processing			
Final particles (no.)	45,299	36,856	63,470
Map resolution (Å) FSC threshold	3.04 0.143	3.84 0.143	3.12 0.143
Model Refinement			
Model resolution (Å) [FSC thresholds]	3.0/3.3 [0.143/0.5]	3.8/6.9 [0.143/0.5]	3.1/3.4 [0.143/0.5]
Mask CC	0.79	0.62	0.78
Volume CC	0.79	0.62	0.78
Map sharpening *B* factor (Å^2) [6]	-40.8	-147.8	-51.1
Model composition			
Non-hydrogen atoms	10,867	9,600	10,052
Protein residues	1,268	1,155	1,150
MgATPs	2	2	2
Drug (VX809)	1	1	1
Lipid molecules	18	8	30
Average *B* factor (Å^2)			
Protein	99.4	149.3	109.1
Ligand molecules	97.1	137.3	130.6
R.m.s. deviations			
Bond lengths (Å)	0.003	0.004	0.003
Bond angles (°)	0.639	0.74	0.64
Validation			
MolProbity score	1.25	1.16	1.22
Clashscore	2.40	1.45	1.86
Poor rotamers (%)	0.0	0.0	0.0
Ramachandran plot			
Favored (%)	96.49	96.05	95.96
Allowed (%)	3.51	3.95	4.04
Disallowed (%)	0.0	0.0	0.00

[1] PHENIX composite map from consensus plus 6 locals (CORE1, AHD1, WalkerB1, CORE2, AHD2, and T2a).
[2] PHENIX composite map from consensus plus 6 locals (CORE1, AHD1, CORE2, AHD2, Walker B2, and T2a).
[3] PHENIX composite map from consensus plus 6 locals (CORE1, AHD1, WalkerB1, CORE2, AHD2, and Walker B2).
[4] After light 2D cleaning of 2,635,244 template-picked particles. 42% (368,526) assigned to CFTR conformations.
[5] After light 2D cleaning of 2,493,670 template-picked particles. 36% (252,534) assigned to CFTR conformations.
[6] Negative of B-factor from Guinier plot for Non-uniform Refinement of consensus map in cryoSPARC.

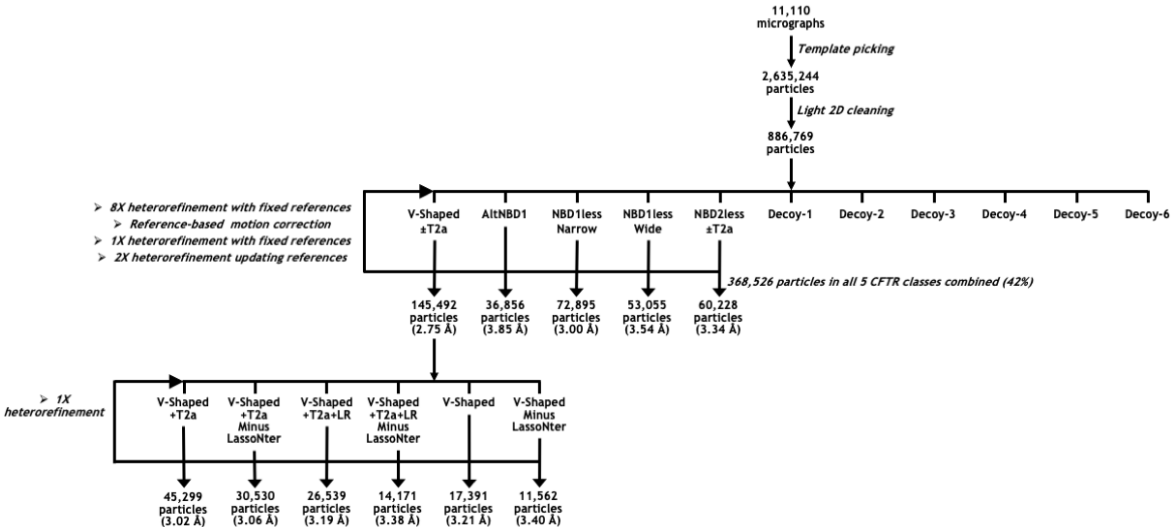

Figure S7. Cryo-EM classification flowchart

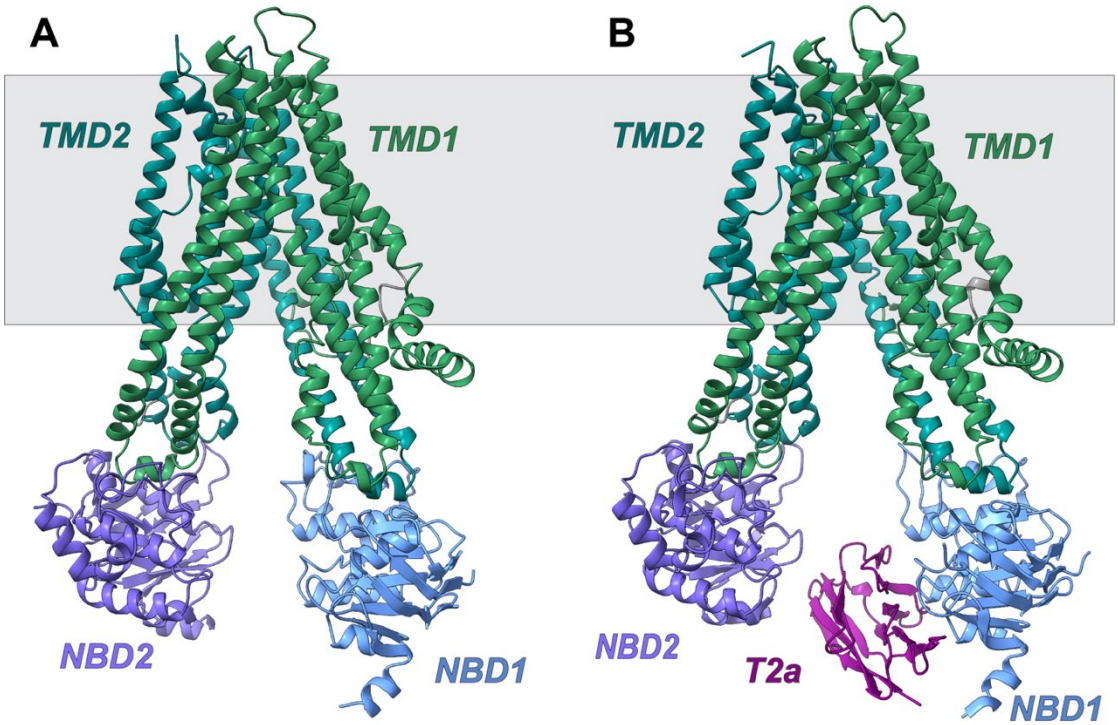

Figure 5. Cryo-EM structures of the "inverted V-shaped" conformation of CFTR in the absence and presence of nanobody T2a

(A) Structure of wt-hCFTR from particles not bound to T2a. TMD1 (comprising helices 1-6) is shown in green ribbon while TMD2 (helices 7-12) is shown in teal with NBD1 in light blue and NBD2 in purple. (B) Structure of the major conformation of CFTR-T2a complex.

The predicted location of the membrane is shown in grey.

Imaging the sample incubated with the nanobody, enabled identification of particles showing density for both CFTR and T2a. Classification led to the identification of at least two distinct conformations (Figures 5-6). The classes corresponding to the major conformation (about 2/3 of the particles) were isolated and enabled 3D reconstruction of a map at a resolution of 3.0 Å leading to straightforward model building of the complex (Figure 5). In this structure, CFTR adopted an inverted V-shaped topology (Figure 5B), with the transmembrane helices adopting a conformation extremely similar to that observed in the apo state found on the same grid (RMSD < 1 Å) (Figure 5A). The structure of the nanobody is clearly visible, and the interface between T2a and NBD1 corresponds closely to that previously identified by X-ray crystallography (Figure S8B) [34]. As a result, the nanobody is located between the two NBDs (Figure 5B) as predicted. However, this position of the nanobody required a slight outward rearrangement of the NBDs when compared to the structure found in the absence of nanobody ("apo" Figure S8C). Minor local rearrangements of the ICLs that connect NBD1 and NBD2 to the TM domains are observed (Figure S8D). These rearrangements appear to allow a rigid-body displacement, which increases the distance between the NBDs by about 6 Å, providing enough space to accommodate the volume of the nanobody which otherwise would clash with NBD2.

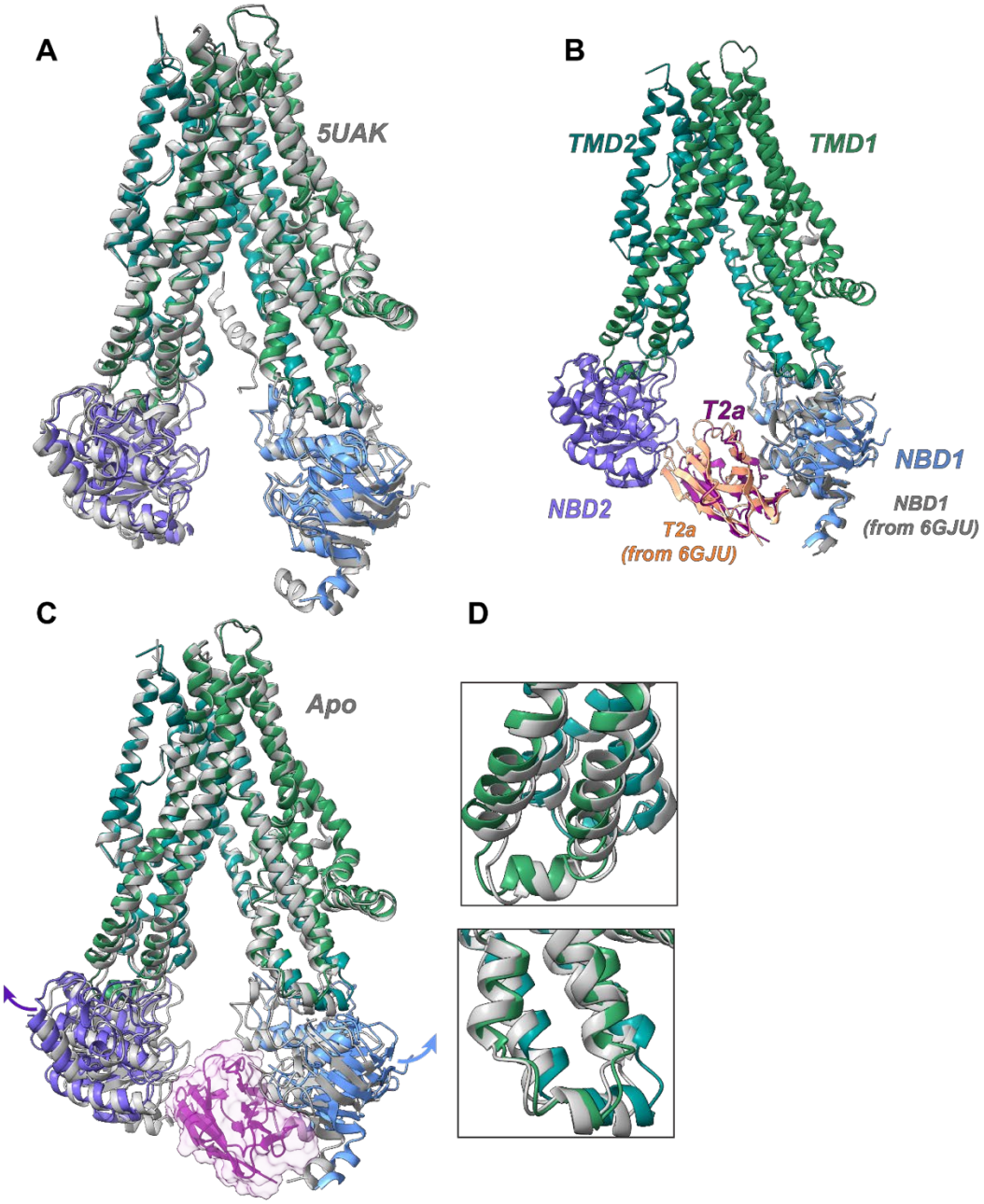

Figure S8. Structural analysis of the inverted V-shaped CFTR structures solved in the absence and presence of T2a nanobody

(A) Superimposition of the apo structure of hCFTR (this work) onto the published structure of dephosphorylated ATP-free hCFTR (PDB id: 5UAK, grey). (B) Superimposition of the NBD1-T2a complex previously obtained by crystallography (PDB id: 6GJU, grey) onto the inverted V-shaped conformation of the full-length CFTR bound to T2a (this work). (C) Superimposition of the inverted V-shaped structures in the absence ("apo", grey) and presence (colored) of T2a, showing the slight motion of the NBDs (arrows). (D) Local rearrangement of the helical loops connecting the TMDs to NBD2 (top) and NBD1 (bottom), respectively.

Both in the absence and presence of T2a, the TM helices of the inverted V-shaped conformation come together on the extracellular side, preventing solvent access to the interior of the TM bundle and ion passage. This observation agrees with analysis previously provided for the dephosphorylated ATP-free hCFTR structure, which concluded that it corresponds to an inactive state as no conduit for desolvated chloride ions was found [51]. Therefore, this T2a-bound conformation likely explains the prolonged closed periods observed in the single-channel recording of wt-CFTR treated with T2a nanobody (Figure 3B and S3).

2D classification of the particles on the cryo-EM grid identified an additional conformation of the CFTR-T2a complex with a large rearrangement of NBD1 and the intracellular region of TMD1 (Figures 6 and S9). While the 2D classes showed molecular details characteristic of high-resolution images, relatively severe preferential orientation of these particles complicated 3D reconstruction but a map of this conformation at 3.9 Å in the consensus region was generated using cycles of iterative anisotropy deconvolution of composite maps, local refinements and composite map synthesis (see Methods). Most of the transmembrane domain structure in this map was directly interpretable, while reference atomic models for the NBDs and T2a nanobody could be readily oriented in the lower resolution regions of the map. This approach enabled an atomic model for the full structure to be built and refined (Figure 6A).

While NBD2 is bound to TMD2 in an equivalent manner to the canonical conformations of CFTR, the NBD1-T2a complex is detached from the intracellular loops of TMD1 and bound instead to the C-terminus of the Lasso motif adjacent to the intracellular surface of the membrane (Figure S9A and B). The transmembrane region of this structure is similar to that observed in the ATP-bound, NBD1/NBD2-associated, chloride-channel formed structure previously reported for the hydrolysis-deficient E1371Q mutant of human CFTR [52] except for the absence of density for ICL4, which comprises the intracellular regions of TM10 and TM11 and the short helix that connects them (Figure S9E). A portion of the volume usually occupied by these two segments shows density for a short α-helical segment likely to be derived from the C-terminus of the R-region based on observation of a continuous connection to the C-terminus of TMD2 in the composite map. Dissociation of NBD1 has been observed previously by cryo-EM, as 2D classes with little or no density for this domain were interpreted to suggest extensive conformational diversity within this region [53].

The position of NBD1 in the novel conformation involves a large-scale translation and rotation compared to the inverted V-shaped structure of hCFTR. NBD1 reorients towards the membrane, rotating along two orthogonal axes (Figure S9B). This movement disrupts all of the standard interactions with ICL1 or ICL4, which, in turn, have somewhat weak density in the novel structure (Figure S9E). The N-terminal antiparallel β-sheet subdomain of NBD1 instead interacts with the Lh2 helix in the C-terminus of the Lasso motif, although the local cryo-EM density in this region is too poor to resolve a detailed view of this new interface. Note that the Lh2 helix is strictly required for CFTR expression [33] and function [54] and contains several rare CF-causing mutations.

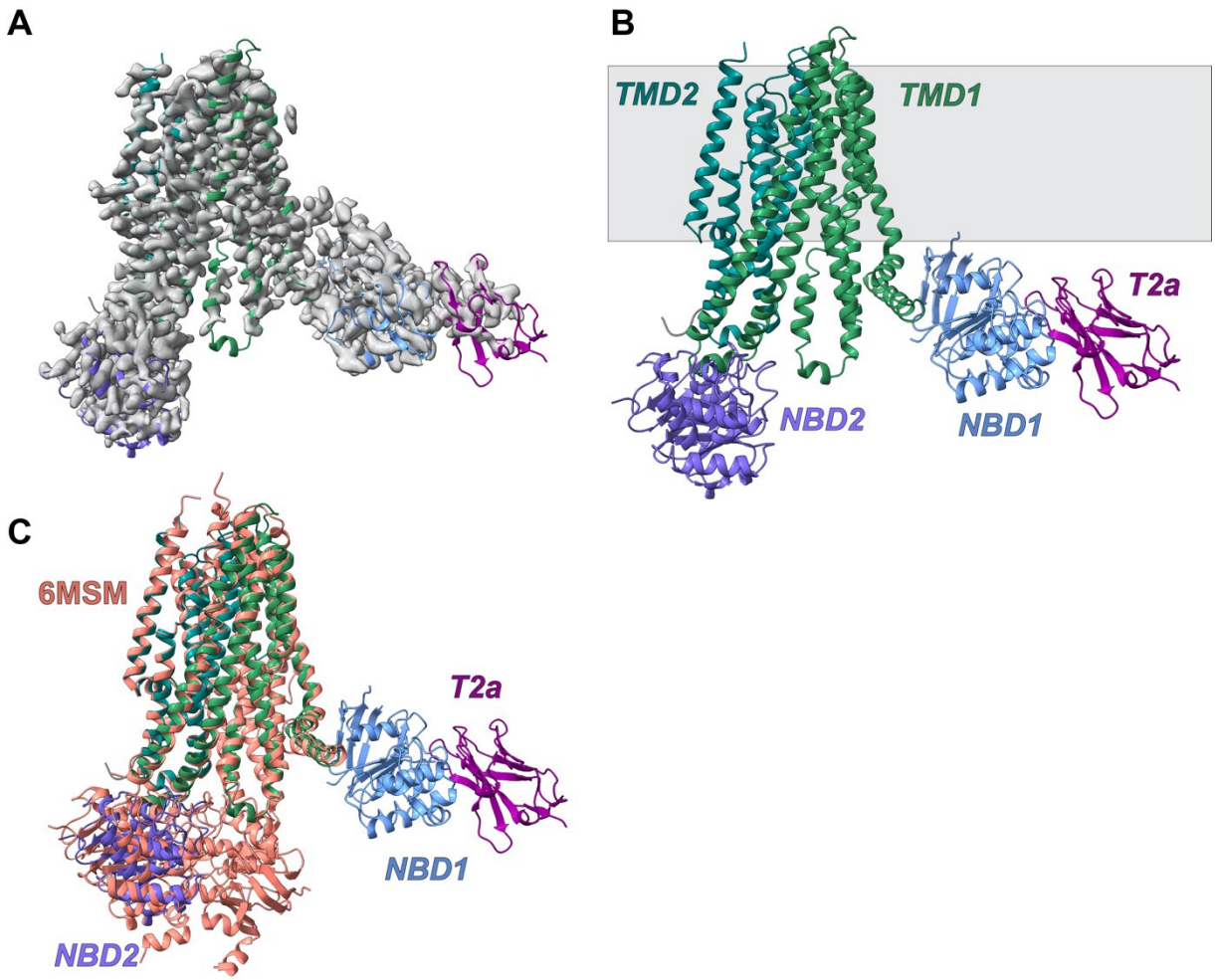

Figure 6. A novel structure of CFTR stabilized by nanobody T2a
(A) EM density for the minor conformation of the CFTR-T2a complex. (B) Atomic model of the novel conformation. The predicted position of the membrane is shown in grey. (C) Structural comparison with the published dephosphorylated ATP-free structure of hCFTR (PDB id: 6MSM, salmon).

As noted above, the TM domain in this novel structure adopts a similar conformation to the previously observed ATP-bound, chloride-channel-formed structure of CFTR (Figure 6C) where the helices in TMD1 and TMD2 come much close to each other on the intracellular side of the membrane and move slightly away from one another on the extracellular side (Figure S9C). When comparing these two structures, we observe that, except for the absence of density for the intracellular regions of TM10 and TM11, as mentioned above, they have very similar conformations, with an overall RSMD ~2 Å. Modest shifts are observed in the position of the intracellular end of TM3 and the extracellular ends of TM10, TM11, and TM12 and ICL1 (Figure S9D and S9E). Analysis of the structure of phosphorylated ATP-bound hCFTR showed an extended Cl^- permeation pathway and, while a fully open channel was not observed, it was proposed that this CFTR conformation was close to that of an active state [52]. Although the limited resolution prevents reliable calculation of a possible ion pathway, the similar organization of TM helices in our novel structure suggests the formation of such an extended Cl^- permeation pathway. We therefore hypothesize that this novel T2a-bound conformation is compatible with the active states observed in our single-channel studies.

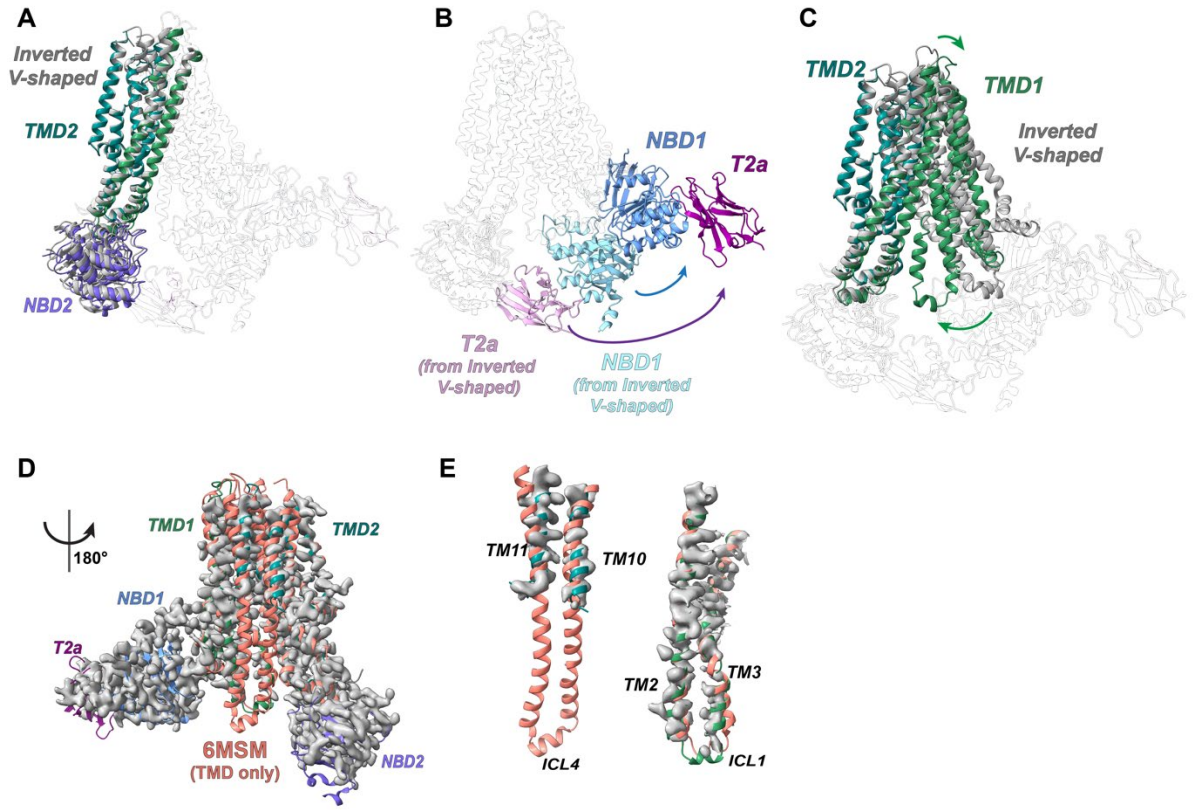

Figure S9. Structural similarities and conformational changes between the inverted V-shaped and the novel conformation of the CFTR-T2a complex

(A) Structural alignment of the NBD2-TMD2 (helices 4, 5, 7, 8, 9, 12) region between the inverted V-shaped (gray) and novel (colored) conformations. For clarity the rest of the protein is represented in transparent ribbons. (B) Using the alignment in (A), a major conformational rearrangement of NBD1 (blue) occurs which unlocks from the TMDs and reorients towards the expected location of the membrane. This motion requires a very large rotation, which is evident from the reorientation of nanobody T2a (purple) in comparison with the inverted V-shaped structure. For clarity the rest of the protein is represented in transparent ribbons. (C) Superimposition of TMD helices from the two T2a-bound structures showing a reorganization of the two halves of the TM bundle, with the helices coming together on the intracellular side and moving slightly apart on the extracellular side. For clarity the rest of the protein is represented in transparent ribbons. (D) Superimposition of the published phosphorylated ATP-bound hCFTR structure (PDB id: 6MSM, salmon) on the novel CFTR-T2a state and its EM density. The NBDs of the published structure have been removed for clarity. (E) Local comparison of the superimposed TM2-ICL1-TM3 and TM10-ICL4-TM11 regions (salmon from 6MSM, green from this work) with corresponding local densities, showing the lack of density within the intracellular parts.

As the novel conformation reported above for the T2a-bound CFTR—featuring an undocked NBD1—has not been reported in previous CFTR structures, it raised the question of whether this state is induced by nanobody binding or can also occur independently. To address this, we analyzed wild-type CFTR particles captured by cryo-EM under conditions identical to those used for the T2a-bound complex, but in the absence of nanobody. Careful inspection revealed a heterogeneous population of conformations, including a subset exhibiting an undocked NBD1 in a

spatial arrangement closely resembling that observed in the T2a-bound structure. While the particle number was insufficient for high-resolution 3D reconstruction, 2D class averages clearly resolved NBD1 in a detached position relative to TMD1, matching the orientation seen in the nanobody-bound complex (Figure S10). Notably, the rest of the channel, including the transmembrane helices, adopted a similar organization, consistent with a channel-formed like architecture. These observations demonstrate that the undocked NBD1 conformation arises in the absence of T2a, supporting its physiological relevance and implicating it as an intrinsic feature of CFTR dynamics, that contribute to the enhanced functional rescue of F508del-CFTR observed with nanobody mRNA-LNP treatment.

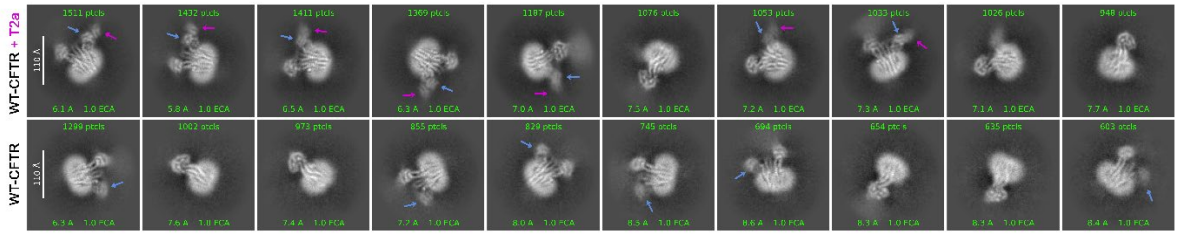

Figure S10. 2D classes with alternative NBD1 binding of WT CFTR cryo-EM datasets collected in the presence (top panel) or absence (bottom) of the T2a nanobody.
The images show the 10 highest-population classes out of 200 total from the final particle stacks for the undocked conformation produced by iterative multi-class heterorefinement**,** refined at 4 Å resolution in cryoSPARC for each dataset. The location of NBD1 and nanobody T2a are highlighted by blue and purple arrows respectively.

DISCUSSION

This study demonstrates that providing CFTR-stabilizing nanobodies to cells expressing F508del-CFTR induces a strong synergy with small-molecule CFTR correctors, leading to a dramatic improvement in F508del-CFTR trafficking and recovery of channel function. This synergy confirms that the approved correctors and the T2a nanobody act via different modes of action.

F508del and other class II mutations affect functional CFTR expression [5], a process which requires a highly complex series of steps including folding of individual domains and their sequential assembly [55] that transforms the newly translated polypeptide into a functional protein at the plasma membrane. The FDA-approved correctors in the ETI combination therapy both bind to TMD1 [30], with tezacaftor lodged in its interface with C-terminus of the Lasso motif [6], while elexacaftor binds between at its interface with the N-terminus of the Lasso motif. These observations have led to the hypothesis that TMD1 serves as a folding platform for NBD1 [6]. Therefore, by binding to the (partially) folded TMDs, the correctors may indirectly help the subsequent folding of F508del-CFTR by stabilizing its folding platform, therefore increasing the overall amount of correctly folded NBD1 and thus the entire channel. It was recently proposed that the folding process of F508del-NBD1 is not affected by temperature, in contrast to the folded state of the domain itself which is temperature sensitive [55]. Therefore, drug-corrected F508del-CFTR may still suffer from thermal instability, limiting the effect of the approved correctors, as observed clinically [20, 26]. Adding a NBD1 stabilizer to the approved correctors should overcome this point of weakness, leading to strong combined effects, as we observed with our T2a nanobody (Figures 1 and 2), which thermally stabilizes NBD1 [34]. This leads to a simple model to explain the remarkable synergy: the approved CFTR correctors help the initial folding steps, including NBD1 (through interaction with TMD1) while binding of T2a to folded NBD1

increases the stability of the partially assembled protein, facilitating the subsequent steps in CFTR folding. As the effects of the small-molecule correctors must precede binding of the stabilizing nanobody, this model explains why we observe little or no effect of T2a on protein maturation in the absence of CFTR correctors (Figures 1 and 2).

The synergistic effects of the NBD1-stabilizing nanobody with CFTR correctors on functional F508del-CFTR expression are consistent with our current understanding of the molecular impact of the mutation. However, the positive effects on channel function that we observed when F508del is thermally protected by T2a led us to revisit and expand models for CFTR activation. The main conformation for the CFTR-T2a complex identified here by cryo-EM fits our original expectation based on the crystal structure of the NBD1-T2a complex (PDB id: 6GJU) [34] and the cryo-EM structure of hCFTR (PDB id: 5UAK) [51] where the location of the nanobody between NBD1 and NBD2 prevents their dimerization, thereby stabilizing the inverted V-shaped conformation in which the internal chloride-conductance channel is not formed (Figure 5B). In parallel, single-channel studies showed that incubation of wt-CFTR with purified T2a leads to extended periods of inactivity (Figures 3B and S3). Such data fully agree with the accepted model where ATP-driven NBD1-NBD2 dimerization is required for channel opening and Cl^- flow [38].

However, the marked increase in F508del-CFTR activity measured with the YFP fluorescence (Figure 2A and B) and Ussing chamber (Figure 2C-H) assays when ETI and the T2a nanobody were combined suggested that the presence of T2a is compatible with channel opening, which was verified using single-channel recording (Figure 3D and E). One simple explanation is that the channel opens only when the nanobody transiently detaches and closes again upon its rebinding. However, this simple model does not account either for the F508del-CFTR activity observed in the presence of saturating nanobody concentrations in single-channel experiments or for the prolonged duration of activity (up to 40 min) in cell-free membrane patches at 37 °C (Figure 3D and E) as thermal protection is strongly suggesting that the nanobody-bound state is predominant during this time period. Moreover, we observed a marked change in the single-channel behavior of F508del-CFTR in the presence of the nanobody, characterized by frequent openings to S-CSs (Figures 4 and S4). Sub-conductance states are very rarely observed with wt-hCFTR (e.g. [56]), but have been observed with mutations that disrupt salt-bridges in the TMDs [57] [47]. The large increase in occurrence of S-CSs when F508del-CFTR is either incubated with purified nanobody or expressed in cells treated with LNPs delivering T2a-encoding mRNA (Figures 4 and S4) clearly indicates that the binding of the nanobody enables such state(s) and therefore must be compatible with channel opening.

The novel conformation of CFTR observed in the CFTR–T2a cryo-EM complex (Figure 6) provides a structural basis for the unexpected functional behavior of F508del-CFTR. In this state, undocking of NBD1 releases the conformational constraint seen in the inverted V-shaped architecture (Figure 5B). Notably, we were able to detect this conformation in cryo-EM grids of wild-type CFTR prepared in the absence of T2a (Figure S10), albeit at low abundance, which precluded high-resolution 3D reconstruction. Our analysis indicates that T2a binding increases the relative population of this state, thereby enriching particle numbers sufficiently to permit EM density reconstruction and atomic modeling of both NBD1 and the nanobody. This suggests that the nanobody does not induce the conformation, but rather stabilizes a naturally occurring, yet transient, structural intermediate of CFTR.

Cryo-EM structures of ABC proteins with incomplete (or missing) NBD domains are typically considered erroneous and thus discarded. However, a few cases of such ABC proteins have been reported, including the bile salt export pump (BSEP/ABCB11) [58] and multidrug resistance protein 4 (MRP4/ABCC4) [59]. Alternatively, poor EM density might denote conformational flexibility. For CFTR, we originally predicted undocking of NBD1 based on recognition of full-length protein by several nanobodies whose epitope (which includes F508) is located at the NBD1-TM1 interface [34] and requires NBD1 displacement before this epitope becomes accessible. Moreover, consistent with

recent evidence supporting the idea of a dynamic NBD1-TM1 interface [55], we have previously reported cryo-EM structures of CFTR with non-visible NBD1, likely due to undocking and subsequent mobility [53].

A consequence of NBD1 undocking is the rearrangement of the TM helices that resembles the conformation of phosphorylated ATP-bound hCFTR [52] which forms a pore-like structure (Figure 6C) suggesting that this novel (T2a-bound) conformation is a conducting state. A striking feature is that, in the absence of NBD1, the EM density shows that the two intracellular regions of TMD1 (on which NBD1 usually docks) are either completely disordered (TM10 and TM11 in ICL4) or weakly ordered (TM2 and TM3 in ICL1 and TM6) indicating enhanced conformational dynamics (Figure S9D and E). These EM map clearly shows a conformation of the TMDs in which the internal chloride-conductance channel has formed, but, because ICL1 and ICL4 in TMD1 are not locked in close proximity to TMD2 by ATP-induced NBD1/NBD2 association, some helices forming the channel are conformationally dynamic. These observations provide a structural framework to interpret the changes in the single-channel behavior of F508del-CFTR as local motion of the helices may lead to sub-optimal pore opening and therefore the observed S-CSs of F508del-CFTR. Consistent with this idea, ivacaftor, which supports both ATP-dependent and ATP-independent channel gating [60, 61] enhanced greatly openings to S-CSs (Figure S4B and C). However, our data suggest that this dynamic pore is also capable of adopting a fully conducting conformation. Indeed, analysis of single-channel records in the presence of the T2a nanobody revealed that F508del-CFTR opens to both sub-conductance and full open states even during prolonged recordings (where F508del-CFTR is typically inactive in the absence of T2a) (Figure 3C-E and S4A-C).

As deletion of F508 is likely to weaken the interface between NBD1 and TMD1 this interaction (cite Chen VX445 paper & Lewis/Hunt/Emtage EMBO J) steric interaction of NBD1-bound T2a and NBD2 (Figure S6C) would be expected to enhance detachment from TMD1 of T2a-bound F508del-NBD1 compared to either T2a-bound WT-NBD1 or T2a-free F508del-NBD1. We hypothesize that this contributes to a greater prevalence of subconductance states arising from NBD1-detached conformations during gating of F508del-CFTR (Figure 4A). This observation supported by the observation that, in marked contrast to wt-CFTR (Figure 3B and S3) no prolonged closed periods of F508del-CFTR occurred in the presence of the nanobody (Figure 3D and E). This result suggests that the T2a-bound inverted V-shaped structure is less stable in F508del-CFTR, likely due to the deletion weakening the NBD1-TMD1 interface.

Our data prove that providing a NBD1-stabilizing molecular chaperone in addition to the approved correctors can improve CFTR function and, and they support the possibility that this approach can be used to ameliorate current CF therapies. We demonstrate that LNPs containing nanobody-encoding mRNA provide an efficient method to deliver a stabilizing molecular chaperone to various cell types. Since ETI does not lead to full recovery of CFTR function, the strength of the combined treatment of approved drugs and stabilizing nanobodies could initiate a new therapeutic strategy for people with CF and F508del and potentially other class II mutations. Of note, when considered with clinical studies which show that ETI restores F508del channel activity to 40 to 50% of that of healthy people [20], our data showing a doubling of CFTR-mediated currents in CFBE cells treated with ETI and T2a suggest that this combination may enhance the rescue of F508del activity towards full restoration (Figure 2). The development of nanobody-based enhancement of pharmacological rescue of F508del-CFTR channel function is attractive on many fronts, including improving the physiological response and decreasing the dosage of correctors, which would helping patients experiencing limited response or intolerance to these drugs. Helped by the dramatic expansion of mRNA-based protein therapies, various delivery strategies access different target organs. For instance, successful nebulization strategies have been developed for mRNA-containing LNPs [40], thus providing a simple and direct administration route for the lungs.

Importantly, we have observed the positive effect of the nanobody in various cell-types, using different functional assays, suggesting that it may be applicable to different tissues and organs. Future studies will be needed to extend this *in-vitro* proof-of-concept to clinically relevant systems, from patient-derived primary cells to preclinical animal models. Therefore, the future points of development will be centered towards developing LNP formulations adapted to such systems, and ultimately to patients [62].

Trafficking diseases have been identified beyond CF and mutations that prevent presence of functional membrane protein at the plasma membrane have been found in an increasing number of cases, affecting proteins of various types, from ABC transporters to GPCRs [63, 64].

While small molecule correctors have been a therapeutic strategy of choice, they might not be applicable to every case or might prove to be of limited efficacy, as for CF where the pharmacological correction remains partial in some patients and poorly tolerated in others [20-22, 24, 26, 27]. The use of target-specific nanobodies as tailored molecular chaperones thus opens a highly complementary therapeutic avenue. The nanobody mRNA-encoding LNPs methodology developed here offers a direct route to provide such customized chaperones to the folding machinery. Considering the demonstrated safety of the LNPs technology for human healthcare [65], the overall strategy can be realistically transformed into therapeutics for CF and other trafficking diseases.

METHODS

Cell culture

HEK293 cells stably heterologously expressing wt or F508del-CFTR with 3 human influenza hemagglutinin (HA)-tags in the fourth extracellular loop [70] were purchased from the Leuven Viral Vector Core. HEK293 cells cultured in DMEM, high glucose, GlutaMAX supplement (Gibco) supplemented with 6% FBS (v v^{-1}) were maintained under puromycin selection at a concentration of 1 µg ml^{-1}. For the HS-YFP assay, CFBE41o$^-$ cells stably heterologously co-expressing F508del-CFTR and HS-YFP [44] were generously provided by Dr. N. Pedemonte. CFBE41o$^-$ expressing F508del-CFTR and HS-YFP cultured in MEM (Gibco) supplemented with 10% FBS (v v^{-1}) and 2 mM L-glutamine were maintained under selection with 2 µg ml^{-1} puromycin and 0.75 mg ml^{-1} geneticin. For Ussing chamber studies, CFBE41o$^-$ stably heterologously expressing F508del-CFTR were kindly supplied by Dr. E. J. Sorscher [67]. CFBE41o$^-$ expressing F508del-CFTR were expanded in MEM supplemented with 10% FBS (v v^{-1}), 5% L-glutamine (v v^{-1}), 100 U ml^{-1} penicillin, 100 U ml^{-1} streptomycin and maintained under puromycin selection at a concentration of 4 µg ml^{-1}. BHK cells stably expressing wt and F508del-CFTR were a generous gift of Dr. M.D. Amaral [68]. They were cultured in a 1:1 mixture of Dulbecco's modified Eagle's Medium and Ham's F-12 nutrient medium supplemented with 5% v v^{-1} fetal calf serum, 100 U ml^{-1} penicillin and 100 µg ml^{-1} streptomycin under methotrexate selection at a concentration of 200 mg ml^{-1}. For structural studies, CFTR protein was expressed in Chinese hamster ovary (CHO) cells. Briefly, the nucleotide sequence of wild-type human CFTR, comprising a C-terminal StrepII-tag was inserted into a lentiviral vector immediately downstream of the tetracycline (Tet)-responsive element (TRE2). This positioned CFTR upstream of an internal ribosome entry site (IRES) followed by an open reading frame comprising puromycin N-acetyl-transferase, T2A and enhanced green fluorescent protein (EGFP), as described earlier [71]. CHO cells constitutively expressing the reverse Tet transactivator (rtTA) were transduced with the packaged CFTR lentiviral vector, and cells expressing EGFP 24 h after treatment with doxycycline were isolated by live-cell FACS sorting. The FACS sorted cells (designated D1557.s) exhibited a stable phenotype over several weeks in culture, including high cell density in large-scale suspension culture and good CFTR expression within 24 h after doxycycline treatment (2 µg ml^{-1}).

All cells were cultured at 37 °C in a humidified atmosphere of 5% CO_2.

Lipid nanoparticles (LNPs) encapsulated T2a mRNA formulation and characterization

T2a-encoding mRNA with N1-methylpseudouridine (m1ψ) modification, Cap-0 and Cap-1 post-transcriptional modification and a 120a-long polyadenylated tail was purchased from Tebu-Bio (Le Perray en Yvelines, France). The T2a nanobody was fused with a C-terminal myc tag (T2a-myc) or an enhanced green fluorescent protein tag (T2a-EGFP). mRNA LNPs were formulated as previously described [72]. Briefly, a lipid mixture composed of D-Lin-MC3-DMA, sitosterol, DMG-PEG 2000, DSPC was prepared in 100% ethanol at 5 mM and a 50:38.5:1.5:10 molar ratio [39, 40] and mRNA was diluted in 50 mM citrate buffer at pH 4.0. The lipid and mRNA solutions were mixed using the microfluidic device NanoAssemblr Ignite (Precision Nanosystems, Cytiva, Vancouver, Canada) at a 1:3 ratio followed by mindialysis for ≥ 90 min against 10% sucrose/PBS using a Slide-A-Lyzer G3 Dialysis Cassette with 10,000 Da molecular-weight cutoff (Thermo Scientific). Hydrodynamic size, polydispersity index and zeta potential were measured with dynamic light scattering using a Zetasizer Nano-ZS (Malvern Instruments, Malvern, UK). Messenger RNA encapsulation efficiency was assayed using the Quant-it RiboGreen RNA Assay Kit (Invitrogen) or QuantiFluor RNA System (Promega).

Sodium dodecyl sulfate-polyacrylamide gel electrophoresis (SDS-PAGE) and immunoblotting

HEK293 or CFBE41o$^-$ cells grown in 3 cm dishes were transfected with T2a-myc or T2a-EGFP mRNA LNPs in DMEM or MEM (Gibco) medium, respectively. Cells were incubated with T2a mRNA LNPs (0.1 to 10 ng µl^{-1}) at least overnight at 37° C concurrently with 3 µM elexacaftor, 18 µM tezacaftor and 3 µM ivacaftor (ETI) or the vehicle DMSO. HEK293 cells were detached with 250 µl EDTA (0.5 mM), while CFBE41o$^-$ cells were detached with 250 µl ice-cold PBS (scrapped) and re-suspended with 3.5 mL medium. 2 mL of cell samples were spun in 2 ml tubes for 5 min at 2,000 x g, 4 °C.

Cell pellets were re-suspended in buffer containing 50 mM Tris-HCl pH 8.0, 150 mM NaCl, 0.1% SDS, 1% Triton X-100, 1 mM PMSF, protease inhibitor cocktail and incubated on ice for at least 1 h with occasional vortexing. Cell lysates were centrifuged for 15 min at 16,000 x g and the protein concentration of the supernatant determined with the Pierce BCA protein assay kit (Thermo Scientific). Proteins were stained with Cy5 N-hydroxysuccinimide ester (Amersham QuickStain Protein Labeling Kit - Cytiva) as a loading control.

Cell extracts were separated by SDS-PAGE on 7.5% polyacrylamide gels and transferred to nitrocellulose membranes (Bio-Rad) for immunodetection. Blots were blocked with 5% bovine serum albumin in Tris-buffered saline with added 0.05% Tween-20 for 1 h. CFTR was detected using monoclonal antibody 596 (1:10,000 - CFTR Antibodies Distribution Program of the Cystic Fibrosis Foundation and the University of North Carolina at Chapel Hill – [43]) and T2a-EGFP was detected using anti-GFP antibody (0.4 µg ml^{-1}, Roche). Antibody binding was detected with anti-mouse HRP conjugated antibody (0.2 µg ml^{-1}, Millipore). The chemiluminescence signal was visualized using Luminata Forte Western HRP substrate (Millipore) and detected with ImageQuant 800 Fluor (Cytiva, Amersham, UK). Densitometry analysis was performed using ImageQuantTL software (Cytiva, Amersham, UK). After subtraction of the background signal, band C intensity was normalized to that of non-transfected cells treated with ETI and the loading control (total protein staining). Statistical significance was calculated by one-way ANOVA implemented in GraphPad Prism 9 (GraphPad Software, San Diego, California, USA, https://www.graphpad.com/).

Flow cytometry

HEK293 cells grown in 3 cm dishes were transfected with T2a-myc or T2a-EGFP mRNA LNPs in DMEM medium (Gibco). Cells were incubated with T2a mRNA LNPs (0.1 to 10 ng µl^{-1}) at least overnight at 37 °C concurrent with 3 µM elexacaftor, 18 µM tezacaftor and 3 µM ivacaftor (ETI) or DMSO. HEK293 cells were detached with 250 µl EDTA (0.5 mM) and re-suspended with 3.5 mL medium. 1.5 mL of cell sample was centrifuged in flow cytometer adapted tubes for 5 min at 200 x g, 4 °C.

Cell pellets were co-incubated with anti-HA tag antibody (2 µg ml^{-1} - BioLegend) and 4´,6-diamidino-2-phenylindole (DAPI - 2.5 µM - Invitrogen) to monitor cell permeabilization. Antibody binding was detected using anti-mouse Alexa Fluor 700 conjugated antibody (1.3 µg mL^{-1} - Invitrogen). The EGFP signal (Ex. 525/50 nm - Em. 500-550 nm), Alexa Fluor 700 signal (Ex. 725/20 nm - Em. 715-735 nm) and the DAPI signal (Ex. 450/50 nm - Em. 425-475 nm) were detected with the Gallios flow cytometer (Beckman Coulter, Brea, California, USA). The Alexa Fluor 700 signal was recorded after gating on cells negative for DAPI (non-permeabilized cells). Data (medians) were analyzed with Kaluza software (Beckman Coulter, Brea, California, USA). Statistical significance was calculated using one-way ANOVA implemented in GraphPad Prism 9 (GraphPad Software, San Diego, California, USA, https://www.graphpad.com/).

Halide-sensitive yellow fluorescent protein (HS-YFP) quenching assay

CFBE41o$^-$ cells stably co-expressing F508del-CFTR and HS-YFP were reverse-transfected with T2a mRNA LNPs (2 ng µl^{-1}) in 96 well plates at least overnight at 37 °C concurrent with elexacaftor (3 µM) and tezacaftor (18 µM) (ET) or DMSO. The day after, cells were stimulated with 10 µM forskolin and potentiated with 3 µM ivacaftor in 200 µl medium for at least 20 min. Fluorescence before and after injection of 5 µl of buffer containing 3 M NaI, 60 mM KI, 38 mM KH_2PO_4, 230 mM Na_2HPO_4*$2H_2O$, 110 mM D-glucose was measured (Ex. 485 nm - Em. 535 nm) with a plate reader SpectraMax iD3 (Molecular Devices, San Jose, California, USA). After subtraction of the baseline (cells without corrector treatment), fluorescence was normalized to that before injection and non-linear regression was obtained with GraphPad Prism 9 (GraphPad Software, San Diego, California, USA, https://www.graphpad.com/). Using the equation of the curve, we obtained the fluorescence 2 seconds after injection. Statistical significance was calculated using one-way ANOVA implemented in GraphPad Prism 9.

Ussing chamber measurements

Preceding treatment, CFBE41o$^-$ cells were trypsinized and passaged at a 1:2 ratio, and puromycin was withdrawn from the medium. The following day, CFBE41o$^-$ cells were again trypsinized and reverse transfected with a solution containing MEM and either T2a mRNA LNPs (20 ng µl^{-1}) or vehicle. Following transfection, one million cells were seeded onto Snapwell filters (Corning). Transfected cultures were maintained as submerged monolayers for 2-3 days. Once transepithelial resistance (R_t) values of ≥ 500 Ω cm^2 with the EVOM^2 epithelial Volt-Ohm-meter were recorded, CFBE41o$^-$ monolayers were treated with either vehicle or elexacaftor (3 µM) and tezacaftor (18 µM) by addition to media bathing the basolateral membrane and incubated for 24 h at 37 °C before mounting in Ussing chambers [73].

Transepithelial short-circuit (I_{sc}) measurements were performed using EasyMount Ussing chambers in a chloride gradient with a voltage clamped to 0 mV as previously described [74]. Briefly, the basolateral compartment was perfused with a solution with the following composition: 145 mM NaCl, 0.4 mM KH_2PO4, 1.6 mM K_2HPO_4, 5 mM D-glucose, 1 mM $MgCl_2$, and 1.3 mM calcium gluconate. The apical compartment was perfused with a 5 mM Cl^- solution containing 5 mM NaCl, 140 mM sodium gluconate, 0.4 mM KH_2PO4, 1.6 mM K_2HPO_4, 5 mM D-glucose, 1 mM $MgSO_4$ and 8 mM calcium gluconate. After a 10-20 min equilibration period in the presence of amiloride (100 µM) added to the solution bathing the apical membrane, CFBE41o$^-$ monolayers were subjected to apical and basolateral treatment with 3-isobutyl-1-methylxanthine (IBMX - 100 µM) and forskolin (10 µM), followed by apical application of ivacaftor (5 µM). Finally, $CFTR_{inh}$-172 (20 µM) was added apically to assess total ion transport through CFTR after activation with forskolin and IBMX and potentiation with ivacaftor; following their addition, all compounds were continuously present in the solution bathing the apical membrane. Statistical analysis was performed by One-Way ANOVA to compare cAMP-induced I_{sc} and $CFTR_{inh}$-172-sensitive I_{sc} between different treatment groups.

Patch-clamp experiments

Prior to study, BHK cells expressing F508del-CFTR were treated with elexacaftor (2 µM) and tezacaftor (3 µM) for 24 h at 37 °C, whereas BHK cells expressing wt-CFTR were untreated. Immediately before commencing single-

channel recordings, F508del-CFTR-expressing cells were washed in drug-free solution to remove CFTR correctors. However, the maximum period cells were left in drug-free solution before study did not exceed 30 min. To test the action of the T2a nanobody on F508del-CFTR, the purified T2a nanobody (1 µM) was added to the intracellular solution bathing excised inside-out membrane patches from BHK cells expressing F508del-CFTR treated with elexacaftor and tezacaftor. Alternatively, F508del-CFTR-expressing BHK cells were transfected with T2a mRNA LNPs (2 ng μl^{-1}) and then incubated with elexacaftor (2 µM) and tezacaftor (3 µM) for 24 h at 37 °C.

CFTR Cl^- channels were recorded in excised inside-out membrane patches from BHK cells heterologously expressing CFTR using an Axopatch 200B patch-clamp amplifier and pCLAMP software (version 10.4) both from Molecular Devices (San Jose, CA) as described previously [75]. The pipette (extracellular) solution contained 140 mM N-methyl-D-glucamine, 140 mM aspartic acid, 5 mM $CaCl_2$, 2 mM $MgSO_4$ and 10 mM N-tris[hydroxymethyl]methyl-2-aminoethanesulfonic acid (TES), adjusted to pH 7.3 with Tris ([Cl^-], 10 mM). The bath (intracellular) solution contained 140 mM NMDG, 3 mM $MgCl_2$, 1 mM CsEGTA and 10 mM TES, adjusted to pH 7.3 with HCl ([Cl^-], 147 mM; free [Ca^{2+}], < 10^{-8} M) and was maintained at 37 °C.

CFTR Cl^- channels were activated promptly following membrane patch excision using the catalytic subunit of protein kinase A (PKA; 75 nM) and ATP (1 mM) before voltage was clamped at –50 mV. Wild-type CFTR was activated at 37 °C, whereas F508del-CFTR was activated at room temperature before temperature was raised to 37 °C once channel activation was complete. To test the effects of purified T2a nanobody protein on the CFTR Cl^- channel, we first recorded single-channel activity for 5 - 10 min in the presence of ATP (wild-type, 0.3 mM; F508del-CFTR, 1 mM) and PKA (75 nM) before adding T2a nanobody (1 µM) to the intracellular solution and acquiring further single-channel activity. For wild-type CFTR, we acquired prolonged recordings in the presence of nanobody T2a, whereas for F508del-CFTR, we acquired 5 - 10 min of single-channel data with nanobody T2a before adding ivacaftor (1 µM) to the intracellular solution and acquiring 30 - 40 min of single-channel data. For F508del-CFTR-expressing cells treated with T2a nanobody mRNA LNPs, following membrane patch excision and channel activation, temperature was raised to 37 °C and 5 - 10 min of single-channel data acquired before ivacaftor (1 µM) was added to the intracellular solution and single-channel data acquired for 30-40 min. To minimize rundown, PKA and ATP were added to all intracellular solutions. On completion of experiments, the recording chamber was thoroughly cleaned before reuse [48]. In this study, we used excised inside-out membrane patches containing ≤ 5 active channels. To determine channel number, we used the maximum number of simultaneous channel openings observed during an experiment determined using conditions that robustly potentiate CFTR activity and recordings that were long enough to ascertain the correct number of channels [76].

Single-channel currents were acquired directly to computer hard disc after filtering at a corner frequency of 500 Hz using an eight-pole Bessel filter (model F-900C/9L8L, Frequency Devices Inc., Ottawa, IL) and digitizing at a sampling rate of 5 kHz using a Digidata 1440A (Molecular Devices) and pCLAMP software. To visualize openings to S-CSs, we digitally filtered single-channel data at 50 Hz using pCLAMP software, excluding transitions < 4 ms from analysis of S-CS events. To measure single-channel current amplitude (i), either Gaussian distributions were fit to current amplitude histograms or cursors were used. For open probability (P_o) measurements of wt CFTR using data digitized at 5 kHz, but not digitally filtered at 50 Hz, lists of open- and closed-times were generated using a half-amplitude crossing criterion for event detection and dwell time histograms constructed as previously described [77]; transitions < 1 ms were excluded from the analysis [eight-pole Bessel filter rise time (T_{10-90}) ~0.73 ms at f_c = 500 Hz]. Histograms were fitted with one or more component exponential functions using the maximum likelihood method. For burst analysis, we used a t_c (the time that separates interburst closures from intraburst closures) determined from closed time histograms [wild-type CFTR control, t_c = 13.26 ± 2.3 ms; wild-type CFTR +

T2a (protein), t_c = 13.03 ± 1.66 ms (n = 4)] [76]. The mean interburst interval (T_{IBI}) was calculated using the equation [76]:

$$P_o = T_b / (T_{MBD} + T_{IBI}) \text{ (Eq. 1)}$$

where T_b = (mean burst duration) x (open probability within a burst). Mean burst duration (T_{MBD}) and open probability within a burst ($P_{o(burst)}$) were determined directly from experimental data using pCLAMP software. Only membrane patches that contained a single active channel were used for burst analyses. For illustration purposes, single-channel records were filtered at 500 Hz and digitized at 5 kHz before file size compression by either 5-fold or 500-fold data reduction using pCLAMP software.

Results are expressed as means ± SEM of n observations, where n represents the number of individual membrane patches obtained from different cells. Using SigmaPlot (version 13.0, Systat Software Inc., San Jose, CA), we tested for differences between 2 groups of data acquired within the same experiment with Student's t-test. Differences were considered statistically significant when $P < 0.05$.

Cryo-EM sample preparation

Methods were equivalent to those previously described for the structural characterization of G551D-6SS-CFTR [53] except for the addition of lumacaftor during tissue culture cell growth. In brief, stable lentiviral transformants of CHO cells verified to produce high level expression of wt-CFTR [69] were solubilized in 0.5% dodecyl-β-D-maltoside (DDM), 0.1% cholesteryl hemisuccinate (CHS), 10% (v v^{-1}) glycerol, 150 mM NaCl, 2 mM DTT, 0.2 mM TCEP, 20 mM HEPES pH 7.5, and Roche cOmplete EDTA-free Protease Inhibitors (Millipore-Sigma, St. Louis, MO). The detergent extract was loaded onto a Strep-Tactin affinity column (IBA LifeSciences, Göttingen, DE), which bound CFTR via a C-terminal Twin-Strep-tag, and then washed extensively with the same buffer containing 0.06% (w v^{-1}) digitonin instead of DDM/CHS prior to elution with 4 mM *d*-desthiobiotin. Purification was completed by two sequential steps of gel-filtration on Superose 6 Increase columns in TNM buffer (0.06% (w v^{-1}) digitonin, 200 mM NaCl, 3 mM $MgCl_2$, 1 mM DTT, 50 mM Tris-Cl pH 7.5). The first was performed on a 10 mm ID column with with 2 mM ATP and 10% (v v^{-1}) glycerol in the buffer, while the second was performed on a 3.2 mm ID microbore column with 150 mM ATP and no glycerol in the buffer. The protein was tumbled at 4 ˚C with TEV protease for 4 h and then PKA for an additional hour prior to the first gel-filtration step. The CFTR monomer peak from the second gel filtration step was concentrated 2-5 fold to a final concentration of ~1.5 mg ml^{-1} and then incubated on ice for 2 h with the T2a nanobody at an ~3:1 ratio (T2a:CFTR) prior to deposition of a 3 µl aliquots on a cryo-EM grid using a Vitrobot Mark IV System (ThermoFisher, Waltham, MA). The T2a nanobody was purified as previously described [34] before transfer by gel filtration to TMN buffer without digitonin and concentrated to ~3 mg ml^{-1} in an Amicon Ultra Centrifugal Filter 10 kDa MWCO (Millipore-Sigma) in a swinging-bucket rotor (14,000 x g). UltraAuFoil 300 mesh R 0.6/1 grids (Quantifoil Inc., UK) were treated for 25 s in a Solarus Plasma Cleaner 950 (Gatan Inc., USA) for 25 s with O_2/H_2 flow-rates of 27.5/6.4 sccm and 15 W cleaning power. Sample deposition and blotting were performed at 4 °C and 100% humidity applying a blot-force of 2-4 with Whatman 1 filter paper (Whatman Inc., Piscataway, NJ) for 6-10 s prior to plunging into liquid ethane.

Cryo-EM data collection

Leginon was used to collect data a 300 kV Titan Krios electron microscope (ThermoFisher Inc., USA) with a K3 camera and imaging filter (Gatan Inc., USA) at the Columbia University Cryo-EM Center using counting mode. The 2.5 s exposures were dose-fractionated into 50 frames. Details are given in Table S1.

Cryo-EM structure determination

Particle classification and 3-dimensional volume reconstructions were performed in cryoSPARC using our previously reported Global Conformational Ensemble Reconstruction methods [78]. In brief, following an exhaustive search for alternative conformations including 3D variability analyses using the full molecular envelope, iterative heterorefinement against the final set of major CFTR conformations and six decoy volumes was performed as schematized in Figure S7 using an initial resolution of 6 Å, followed by *ab inito* reconstruction and then non-uniform refinement of the particles assigned to each conformational class. Following generation of consensus maps for each structure in cryoSPARC, local refinements were performed on the two NBDs separately or on NBD1 and T2a together for the structures containing T2a. The outputs from those initial local refinements were used as inputs for an additional round of local refinements in smaller masks covering internally rigid structures that rotate relative to one another (i.e., T2a, the ATP-binding core subdomain and the alpha-helical subdomain in both NBDs, the alpha-helix following the Walker B motif in NBD2, and, exclusively for the V-Shaped structure, the equivalent alpha-helix in NBD1. Gaussian rotation and translation restraints in ranges from 0-4 degrees and 0-4 pixels, respectively, were used for all local refinements, with the magnitudes being determined empirically by trial-and-error based on inspection of the output density maps. Composite map and half-map generation were performed in PHENIX using local weighting to a coordinate model after manual alignment of all local maps and half maps to the consensus full map in ChimeraX. The coordinate model used for composite map generation was produced by one round of real-space refinement in PHENIX against a crude manual composite map made from the aligned consensus and local maps using the Volume Maximum function in ChimeraX. For the AltNBD1 map, the initial composite map from cryoSPARC was used as input for anisotropy deconvolution in ARDECON with parameters optimized as recommended [79], and the PHENIX model-sharpened map from that procedure was used to seed non-uniform refinement in cryoSPARC to generate a new consensus map. That updated consensus map, which showed somewhat reduced orientational bias compared to the original consensus map, was used for another round of local refinements in cryoSPARC and composite map generation in PHENIX. These sequential ARDECON, local refinement, and composite map generation procedures were repeated two additional times to produce the final AltNBD1 composite map (Figure 6 and Table S1). Manual model rebuilding was performed using COOT [80] based on previously published structures [51, 52] and real-space refinement of coordinate models and model-validation calculations were performed in PHENIX .

Data Presentation

Structural figures were generated using UCSF ChimeraX. Plots were generated using GraphPad Prism 9. Flow cytometry histogram overlays were generated with FlowJo. All the figures were assembled using Adobe Illustrator.

QUANTIFICATION AND STATISTICAL ANALYSIS

The quantification and statistical analyses are integral parts of the algorithms used. Details are described in the main text and methods sections.

SUPPLEMENTAL DOCUMENT

T2a mRNA sequence

ATGCAGGTGCAGCTGCAGGAGTCAGGAGGAGGACTGGTGCAGGCAGGAGGATCTCTGAGACTGTCTTGCGCCGCTAGCG
GCAGCATCTTTAGGATCGACGCTATGGGCTGGTACAGGCAGGCCCCAGGAAAACAGAGAGAGCTGGTGGCTCACAGCACA
AGCGGAGGCAGCACCGATTACGCCGATAGCGTGAAGGGCAGGTTCACCATCAGCCGGGACAACGCCAAGAACACCGTGTA
CCTGCAGATGAACAGCCTGAAGCCCGAGGACACCGCCGTGTACTATTGCAACGCCGACGTGCGAACCCGCTGGTACGCCAG
CAACAACTACTGGGGACAGGGAACACAGGTCACCGTGTCTAGCGGAAGCGGATCT

RESOURCE AVAILABILITY

Lead contact

Requests regarding reagents and further information may be addressed to the lead contact, Cedric Govaerts (cedric.govaerts@ulb.be).

Materials availability

This study did not generate new unique reagents.

Data and code availability

- The cryo-EM movies used to generate the structures reported in this paper have been deposited in EMPIAR (EMPIAR-12127 and EMPIAR-12947). All consensus, local, and composite maps have been deposited in the EMDB (EMD-71756, EMD-71757, EMD-71758, EMD-71759, EMD-71760, EMD-71761, EMD-71762, EMD-71763, EMD-71764, EMD-71765, EMD-72403, EMD-71756, EMD-71757, EMD-71758, EMD-71759, EMD-71760, EMD-71761, EMD-71762, EMD-71763, EMD-71764, EMD-71765, EMD-72403, EMD-72491, EMD-72492, EMD-72493, EMD-72494, EMD-72495, EMD-72496, EMD-72356, EMD-72497), and the corresponding coordinate models have been deposited in the PDB (9Q1W, 9Y1Q, and 9Y4T) for public release at the time of publication.
- Any additional information required to analyze the data reported in this paper is available from the lead contact upon request.
- This paper does not report original code.

AUTHOR CONTRIBUTIONS

M.O. performed the CFTR maturation experiments and the HS-YFP quenching assays and analyzed the data with assistance of C.G. M.O. provided nanobodies and LNPs samples for Ussing chamber, patch-clamp and cryo-EM experiments. T.R. performed Ussing chamber measurements and analyzed the data with assistance of A.B. J.N.C. and M.R. carried out patch-clamp experiments and analyzed the data with assistance of D.N.S. A.S.P., B.L. and Z.R

performed cryo-EM experiments and analyzed the data with assistance of J.F.H. and C.G. Z.Y. prepared CFTR samples for cryo-EM experiments. J.C.K. provided stable cell line for CFTR expression. M.O., T.R., J.N.C., M.R., A.B., M.A.M., D.N.S., J.F.H., C.G. contributed to writing the manuscript. C.G. oversaw the project.

ACKNOWLEDGMENTS

We thank A. des Rieux and F. Debuisson for their excellent assistance for LNPs formulation, K. Seidel and M. Drescher for their expert technical support, J. Baranwal and L. Prasad for assistance generating composite cryoEM maps and refining the coordinate models, and Kathrin Seidel and Marika Drescher for expert technical support with cell culture and H. Remaut for valuable comments on the manuscript. This work was supported by (i) C.G.: the Fonds Forton, the Welbio (grant CR-2012S-04R), the Association luxembourgeoise de la lutte contre la mucoviscidose, the CF Trust, the Fondation Air Liquide and the Fondation ULB; (ii) D.N.S: the CF Trust (SRC 021); (iii) J.F.H. is grateful for 25 years of financial support from the US Cystic Fibrosis Foundation. (iv) J.C.K.: the Cystic Fibrosis Foundation (KAPPES18XX0, KAPPES20XX0) and (v) M.A.M.: the German Research Foundation (CRC 1449 – 431232613, 450557679 to M.A.M.) and the German Federal Ministry of Education and Research (82DZL009C1 and 01GL2401A to M.A.M.). C.G. is a senior Research Associate of the FRS-FNRS and a WELRI Investigator. J.N.C. is a CF Trust-supported PhD student (SRC 024).

REFERENCES

1. De Matteis, M.A. and Luini, A. (2011) Mendelian disorders of membrane trafficking. N Engl J Med 365 (10), 927-38.
2. Cutting, G.R. (2015) Cystic fibrosis genetics: from molecular understanding to clinical application. Nat Rev Genet 16 (1), 45-56.
3. Mall, M.A. et al. (2024) Cystic fibrosis. Nat Rev Dis Primers 10 (1), 53.
4. Riordan, J.R. et al. (1989) Identification of the cystic fibrosis gene: cloning and characterization of complementary DNA. Science 245 (4922), 1066-73.
5. Veit, G. et al. (2016) From CFTR biology toward combinatorial pharmacotherapy: expanded classification of cystic fibrosis mutations. Mol Biol Cell 27 (3), 424-33.
6. Kleizen, B. et al. (2021) Co-Translational Folding of the First Transmembrane Domain of ABC-Transporter CFTR is Supported by Assembly with the First Cytosolic Domain. J Mol Biol 433 (13), 166955.
7. Kim, S.J. and Skach, W.R. (2012) Mechanisms of CFTR Folding at the Endoplasmic Reticulum. Front Pharmacol 3, 201.
8. Protasevich, I. et al. (2010) Thermal unfolding studies show the disease causing F508del mutation in CFTR thermodynamically destabilizes nucleotide-binding domain 1. Protein Sci 19 (10), 1917-31.
9. Wang, C. et al. (2010) Integrated biophysical studies implicate partial unfolding of NBD1 of CFTR in the molecular pathogenesis of F508del cystic fibrosis. Protein Sci 19 (10), 1932-47.
10. Cheng, S.H. et al. (1990) Defective intracellular transport and processing of CFTR is the molecular basis of most cystic fibrosis. Cell 63 (4), 827-34.
11. Thibodeau, P.H. et al. (2010) The cystic fibrosis-causing mutation ΔF508 affects multiple steps in cystic fibrosis transmembrane conductance regulator biogenesis. J Biol Chem 285 (46), 35825-35.
12. Denning, G.M. et al. (1992) Processing of mutant cystic fibrosis transmembrane conductance regulator is temperature-sensitive. Nature 358 (6389), 761-4.
13. He, L. et al. (2015) Restoration of NBD1 thermal stability is necessary and sufficient to correct ΔF508 CFTR folding and assembly. J Mol Biol 427 (1), 106-20.

14. Pissarra, L.S. et al. (2008) Solubilizing mutations used to crystallize one CFTR domain attenuate the trafficking and channel defects caused by the major cystic fibrosis mutation. Chem Biol 15 (1), 62-9.
15. Rabeh, W.M. et al. (2012) Correction of both NBD1 energetics and domain interface is required to restore ΔF508 CFTR folding and function. Cell 148 (1-2), 150-63.
16. Mendoza, J.L. et al. (2012) Requirements for efficient correction of ΔF508 CFTR revealed by analyses of evolved sequences. Cell 148 (1-2), 164-74.
17. Keating, D. et al. (2018) VX-445-Tezacaftor-Ivacaftor in Patients with Cystic Fibrosis and One or Two Phe508del Alleles. N Engl J Med 379 (17), 1612-1620.
18. Middleton, P.G. et al. (2019) Elexacaftor-Tezacaftor-Ivacaftor for Cystic Fibrosis with a Single Phe508del Allele. N Engl J Med 381 (19), 1809-1819.
19. Heijerman, H.G.M. et al. (2019) Efficacy and safety of the elexacaftor plus tezacaftor plus ivacaftor combination regimen in people with cystic fibrosis homozygous for the F508del mutation: a double-blind, randomised, phase 3 trial. Lancet 394 (10212), 1940-1948.
20. Graeber, S.Y. et al. (2022) Effects of Elexacaftor/Tezacaftor/Ivacaftor Therapy on CFTR Function in Patients with Cystic Fibrosis and One or Two F508del Alleles. Am J Respir Crit Care Med 205 (5), 540-549.
21. Schaupp, L. et al. (2023) Longitudinal effects of elexacaftor/tezacaftor/ivacaftor on sputum viscoelastic properties, airway infection and inflammation in patients with cystic fibrosis. Eur Respir J 62 (2), e2202153.
22. Morgan, S.J. et al. (2024) Elexacaftor/tezacaftor/ivacaftor's effects on cystic fibrosis infections are maintained, but not increased, after 3.5 years of treatment. J Clin Invest 134 (20), e184171.
23. Hirtz, S. et al. (2004) CFTR Cl- channel function in native human colon correlates with the genotype and phenotype in cystic fibrosis. Gastroenterology 127 (4), 1085-95.
24. Nichols, D.P. et al. (2023) Pharmacologic improvement of CFTR function rapidly decreases sputum pathogen density, but lung infections generally persist. J Clin Invest 133 (10), e167957.
25. Casey, M. et al. (2023) Effect of elexacaftor/tezacaftor/ivacaftor on airway and systemic inflammation in cystic fibrosis. Thorax 78 (8), 835-839.
26. Armbruster, C.R. et al. (2024) Persistence and evolution of Pseudomonas aeruginosa following initiation of highly effective modulator therapy in cystic fibrosis. mBio 15 (5), e0051924.
27. Lieu, N. et al. (2023) Trials and tribulations of highly effective modulator therapies in cystic fibrosis. Paediatr Respir Rev 48, 10-19.
28. Graeber, S.Y. and Mall, M.A. (2023) The future of cystic fibrosis treatment: from disease mechanisms to novel therapeutic approaches. Lancet 402 (10408), 1185-1198.
29. Alicandro, G. et al. (2024) Heterogeneity in response to Elexacaftor/Tezacaftor/Ivacaftor in people with cystic fibrosis. J Cyst Fibros 23 (6), 1072-1079.
30. Fiedorczuk, K. and Chen, J. (2022) Molecular structures reveal synergistic rescue of Δ508 CFTR by Trikafta modulators. Science 378 (6617), 284-290.
31. Liu, F. et al. (2019) Structural identification of a hotspot on CFTR for potentiation. Science 364 (6446), 1184-1188.
32. Fiedorczuk, K. and Chen, J. (2022) Mechanism of CFTR correction by type I folding correctors. Cell 185 (1), 158-168.e11.
33. Sabusap, C.M. et al. (2021) The CFTR P67L variant reveals a key role for N-terminal lasso helices in channel folding, maturation, and pharmacologic rescue. J Biol Chem 296, 100598.
34. Sigoillot, M. et al. (2019) Domain-interface dynamics of CFTR revealed by stabilizing nanobodies. Nat Commun 10 (1), 2636.
35. Scholl, D. et al. (2021) A topological switch in CFTR modulates channel activity and sensitivity to unfolding. Nat Chem Biol 17 (9), 989-997.
36. Jovčevska, I. and Muyldermans, S. (2020) The Therapeutic Potential of Nanobodies. BioDrugs 34 (1), 11-26.
37. Peyvandi, F. et al. (2016) Caplacizumab for Acquired Thrombotic Thrombocytopenic Purpura. N Engl J Med 374 (6), 511-22.

38. Vergani, P. et al. (2005) CFTR channel opening by ATP-driven tight dimerization of its nucleotide-binding domains. Nature 433 (7028), 876-80.
39. Robinson, E. et al. (2018) Lipid Nanoparticle-Delivered Chemically Modified mRNA Restores Chloride Secretion in Cystic Fibrosis. Mol Ther 26 (8), 2034-2046.
40. Kim, J. et al. (2022) Engineering Lipid Nanoparticles for Enhanced Intracellular Delivery of mRNA through Inhalation. ACS Nano 16 (9), 14792-14806.
41. Illek, B. et al. (2008) Cl transport in complemented CF bronchial epithelial cells correlates with CFTR mRNA expression levels. Cell Physiol Biochem 22 (1-4), 57-68.
42. Ehrhardt, C. et al. (2006) Towards an in vitro model of cystic fibrosis small airway epithelium: characterisation of the human bronchial epithelial cell line CFBE41o. Cell Tissue Res 323 (3), 405-15.
43. Cui, L. et al. (2007) Domain interdependence in the biosynthetic assembly of CFTR. J Mol Biol 365 (4), 981-94.
44. Sondo, E. et al. (2011) Rescue of the mutant CFTR chloride channel by pharmacological correctors and low temperature analyzed by gene expression profiling. Am J Physiol Cell Physiol 301 (4), C872-85.
45. Galietta, L.V. et al. (2001) Cell-based assay for high-throughput quantitative screening of CFTR chloride transport agonists. Am J Physiol Cell Physiol 281 (5), C1734-42.
46. Scott-Ward, T.S. et al. (2007) Chimeric constructs endow the human CFTR Cl- channel with the gating behavior of murine CFTR. Proc Natl Acad Sci U S A 104 (41), 16365-70.
47. Cui, G. et al. (2013) Two salt bridges differentially contribute to the maintenance of cystic fibrosis transmembrane conductance regulator (CFTR) channel function. J Biol Chem 288 (28), 20758-67.
48. Meng, X. et al. (2017) Two Small Molecules Restore Stability to a Subpopulation of the Cystic Fibrosis Transmembrane Conductance Regulator with the Predominant Disease-causing Mutation. J Biol Chem 292 (9), 3706-3719.
49. Punjani, A. and Fleet, D.J. (2021) 3D variability analysis: Resolving continuous flexibility and discrete heterogeneity from single particle cryo-EM. J Struct Biol 213 (2), 107702.
50. Punjani, A. et al. (2020) Non-uniform refinement: adaptive regularization improves single-particle cryo-EM reconstruction. Nat Methods 17 (12), 1214-1221.
51. Liu, F. et al. (2017) Molecular Structure of the Human CFTR Ion Channel. Cell 169 (1), 85-95.e8.
52. Zhang, Z. et al. (2018) Molecular structure of the ATP-bound, phosphorylated human CFTR. Proc Natl Acad Sci U S A 115 (50), 12757-12762.
53. Wang, C. et al. (2022) Mechanism of dual pharmacological correction and potentiation of human CFTR. bioRxiv, 2022.10. 10.510913.
54. Naren, A.P. et al. (1999) CFTR chloride channel regulation by an interdomain interaction. Science 286 (5439), 544-8.
55. van der Sluijs, P. et al. (2024) The Folding Pathway of ABC Transporter CFTR: Effective and Robust. J Mol Biol 436 (14), 168591.
56. Cai, Z. et al. (2003) Voltage-dependent gating of the cystic fibrosis transmembrane conductance regulator Cl- channel. J Gen Physiol 122 (5), 605-20.
57. Cotten, J.F. and Welsh, M.J. (1999) Cystic fibrosis-associated mutations at arginine 347 alter the pore architecture of CFTR. Evidence for disruption of a salt bridge. J Biol Chem 274 (9), 5429-35.
58. Liu, H. et al. (2023) Structural basis of bile salt extrusion and small-molecule inhibition in human BSEP. Nat Commun 14 (1), 7296.
59. Pourmal, S. et al. (2024) Structural basis of prostaglandin efflux by MRP4. Nat Struct Mol Biol 31 (4), 621-632.
60. Eckford, P.D. et al. (2012) Cystic fibrosis transmembrane conductance regulator (CFTR) potentiator VX-770 (ivacaftor) opens the defective channel gate of mutant CFTR in a phosphorylation-dependent but ATP-independent manner. J Biol Chem 287 (44), 36639-49.
61. Jih, K.Y. and Hwang, T.C. (2013) Vx-770 potentiates CFTR function by promoting decoupling between the gating cycle and ATP hydrolysis cycle. Proc Natl Acad Sci U S A 110 (11), 4404-9.

62. Beerepoot, P. et al. (2017) Pharmacological chaperone approaches for rescuing GPCR mutants: Current state, challenges, and screening strategies. Pharmacol Res 117, 242-251.
63. Marinko, J.T. et al. (2019) Folding and Misfolding of Human Membrane Proteins in Health and Disease: From Single Molecules to Cellular Proteostasis. Chem Rev 119 (9), 5537-5606.
64. Moore, J.M. et al. (2023) ABC transporters: human disease and pharmacotherapeutic potential. Trends Mol Med 29 (2), 152-172.
65. Baden, L.R. et al. (2024) Long-term safety and effectiveness of mRNA-1273 vaccine in adults: COVE trial open-label and booster phases. Nat Commun 15 (1), 7469.
66. Bebok, Z. et al. (2005) Failure of cAMP agonists to activate rescued deltaF508 CFTR in CFBE41o- airway epithelial monolayers. J Physiol 569 (Pt 2), 601-15.
67. Gottschalk, L.B. et al. (2016) Creation and characterization of an airway epithelial cell line for stable expression of CFTR variants. J Cyst Fibros 15 (3), 285-94.
68. Farinha, C.M. et al. (2002) The human DnaJ homologue (Hdj)-1/heat-shock protein (Hsp) 40 co-chaperone is required for the in vivo stabilization of the cystic fibrosis transmembrane conductance regulator by Hsp70. Biochem J 366 (Pt 3), 797-806.
69. Yang, Z. et al. (2018) Structural stability of purified human CFTR is systematically improved by mutations in nucleotide binding domain 1. Biochim Biophys Acta Biomembr 1860 (5), 1193-1204.
70. Sharma, M. et al. (2004) Misfolding diverts CFTR from recycling to degradation: quality control at early endosomes. J Cell Biol 164 (6), 923-33.
71. Hildebrandt, E. et al. (2015) Erratum to: A Stable Human-Cell System Overexpressing Cystic Fibrosis Transmembrane Conductance Regulator Recombinant Protein at the Cell Surface. Mol Biotechnol 57 (5), 406.
72. Patel, S. et al. (2017) Boosting Intracellular Delivery of Lipid Nanoparticle-Encapsulated mRNA. Nano Lett 17 (9), 5711-5718.
73. Balázs, A. et al. (2025) The potentiator ivacaftor is essential for pharmacological restoration of F508del-CFTR function and mucociliary clearance in cystic fibrosis. JCI Insight 10 (10), e187951.
74. Balázs, A. et al. (2022) Age-Related Differences in Structure and Function of Nasal Epithelial Cultures From Healthy Children and Elderly People. Front Immunol 13, 822437.
75. Cai, Z. et al. (2015) Impact of the F508del mutation on ovine CFTR, a Cl- channel with enhanced conductance and ATP-dependent gating. J Physiol 593 (11), 2427-46.
76. Cai, Z. et al. (2006) Differential sensitivity of the cystic fibrosis (CF)-associated mutants G551D and G1349D to potentiators of the cystic fibrosis transmembrane conductance regulator (CFTR) Cl- channel. J Biol Chem 281 (4), 1970-7.
77. Sheppard, D.N. and Robinson, K.A. (1997) Mechanism of glibenclamide inhibition of cystic fibrosis transmembrane conductance regulator Cl- channels expressed in a murine cell line. J Physiol 503 (Pt 2) (Pt 2), 333-46.
78. Li, Y. et al. (2022) Oligomeric interactions maintain active-site structure in a noncooperative enzyme family. Embo j 41 (17), e108368.
79. Li, J. et al. (2025) Deconvolution to restore cryo-EM maps with anisotropic resolution. bioRxiv, 2025.02.23.639707.
80. Casañal, A. et al. (2020) Current developments in Coot for macromolecular model building of Electron Cryo-microscopy and Crystallographic Data. Protein Sci 29 (4), 1069-1078.